CENTRO DE INVESTIGACIONES
EN OPTICA, A.C.

“POLYMER CAPPED OPTICAL FIBER TIPS FOR SENSING”

Tesis que para obtener el grado de Doctor en Ciencias (Óptica)

Presenta: M. C. Miguel Ángel Ramírez Hernández

Director de Tesis: Dr. David Monzón Hernández

León · Guanajuato · México

Enero de 2025

To my wife and soulmate, Yesenia,
my brother and best friend, Luis,
and my parents and heroes, Mercedes and Miguel.

ACKNOWLEDGMENTS

I want to acknowledge CONAHCYT for my PhD scholarship (No. CVU: 742457) and their financial support.

Thanks to Centro de Investigaciones en Óptica (CIO) for the opportunity to earn my Master's and PhD degrees and the facilities to carry out this research work.

I thankfully acknowledge the support that I received from Dra. Verónica Vázquez, Dr. Alexander Kiryanov, and Dr. Olivier Pottiez, for their time and effort during the development of this thesis work as my evaluating committee.

I sincerely thank Dr. David Monzón for his support, guidance, and mentoring. Besides, for accepting me in his group and allowing me to continue my PhD.

I am deeply grateful to my family. My gorgeous wife, Yesenia, who always accompanied me on this bumpy road, supporting and motivating me to continue and with whom I am infinitely in love. My brother and the best man I've ever met, Luis, who was always present in my sleepless nights. My loving and beautiful mother, Mercedes, who taught me the most fundamental aspects of life and always took care of me with unconditional love. My brave father, Miguel, who, with his example, made me the man I am today. And my loyal friend, Alí, who reminds me every day that I must not stop smiling.

An acknowledgment to my CIO friends: Edgar, Chago, Pipe, and Brandon. For his friendship and for helping me have an unforgettable stay at the CIO.

Thanks to all members of GSOM for their teachings and companionship that they gave me in the laboratory mornings.

A special acknowledgment to Ing. Juan Carlos Rodriguez Márquez from the mechanical workshop department and M. E. Ricardo Valdivia Hernández from the Optomechatronic laboratory for their special support in this work. Also, thanks to all members of both groups and all the people of the academic department, janitorial, security guards, and every staff that makes the CIO work.

ABSTRACT

Attaching sensitive materials to the tip of an optical fiber has proven to be a practical approach for creating selective and highly sensitive sensors. In this thesis, I report the fundamentals to design, fabricate and characterize displacement and temperature sensors, based on a modified extrinsic Fabry Pérot interferometer, by adding a semi-spherical polymer cap to the end face of an SMF FC/PC connector. The displacement sensor presents a dynamic range 9 times larger than that obtained with an extrinsic fiber Fabry-Perot interferometer (EFFPI), besides a subnanometer resolution was demonstrated, taking advantage of the optical Vernier effect. The temperature sensor shows a 69 times temperature sensitivity improvement with respect to a conventional EFFPI with a polymer cap by implementing the Vernier effect in a double-cavity Fabry-Perot interferometer (DCFPI) configuration. I also propose a sensor package consisting of a machined movable mount. These sensors possess characteristics that could be attractive for some applications, such as the robustness provided by the connector, the simple fabrication process, or the detection of minimal changes in position or temperature measures. I designed, developed, and implemented an automated mechatronic platform to fabricate the polymer-caped fiber Fabry-Pérot interferometer (PCFPI) tips.

CONTENTS

CHAPTER 1:
INTRODUCTION

The Handbook of modern sensors [1] presents a brief but accurate definition of a sensor:

"A sensor is a device that receives a stimulus and responds with an electrical signal."

The stimulus, also known as measurand, is the input variable of any sensing system. It is the physical property received and converted into an electrical signal, which can be channeled, amplified, and modified. After such a transition, we can call it an output signal.

There is a wide variety of sensor classifications. This work first considers direct and complex sensors. A direct sensor transforms a stimulus into an electrical signal by employing a specific physical effect. In contrast, a complex sensor uses one or more energy transducers before a direct sensor generates an electrical output. The difference between a sensor and a transducer is that the former converts any energy into electrical energy, and the latter converts any energy into another.

A modern sensor is an extensive system of components, including detectors, signal conditioners, processors, memory devices, data recorders, and actuators. An actuator is the opposite of a sensor; it converts electric energy into generally nonelectrical energy.

It is challenging to accurately pinpoint the first modern sensor in history due to the evolution of the concept of sensors and their applications. However, if we consider a system able to detect, measure, and convert physical magnitudes from any domain to an electrical domain, the thermocouple by Thomas Seebeck was the first device to approach this definition. In August 1821, Seebeck published his discovery that two different metals forming a closed circuit will display magnetic properties when there is a temperature difference between the two points of contact. Thus, the Seebeck effect is the basis of thermoelectricity and has led to the development of thermocouples for contact temperature measurement [2].

Light is a very efficient form of energy for sensing various stimuli, such as distance, motion, temperature, chemical composition, and many others. Optical sensors offer advantages over typical sensors, including their insensitivity to stray magnetic fields or electrostatic interferences, non-contact operation, the absence of loading effect, and more. The first electro-optical sensing system in history was the photophone by Alexander Graham Bell and his assistant, Sumner Tainter, in 1880. The photophone uses a selenium photodetector, which converts luminous energy into voltage to be transformed into acoustic signals by a telephone [3]. It was a stunning advance in optical communication technology; the photophone could transmit a human voice hundreds of meters on a light beam. This invention was the basis for developing communications using fiber optics and lasers years later. First, the laser was invented in 1960 by Theodore Maiman at Hughes Research Labs, where he developed the ruby laser for the first time [4]. On the other hand, fiber optics were first demonstrated in 1970 when Robert Maurer, Donald Keck, and Peter Schultz, researchers at Corning Glass, developed the first single-mode glass fiber with attenuation below 20 dB/km [5].

Beyond the communication technology revolution caused by the laser and fiber optic inventions, both devices formed the basis of many optical systems, including multiple sensors, specifically Optical Fiber Sensors (OFS). The first history sensor based on fiber

optics was the optical fiber hydrophone. This sensitive acoustic detector uses the phase modulation of an optical beam in a submerged optical fiber by soundwaves propagating in a fluid [1977]. Fiber optic sensors are classified into five basic categories [1]:

- Intensity-modulated sensors.
- Phase-modulated sensors.
- Wavelength-modulated sensors.
- Scattering-based sensors.
- Polarization-based sensors.

Intensity-modulated sensors use the fiber or a mechanical transducer attached to another fiber to interact with physical perturbations. This perturbation produces a change in the received light intensity, being a function of the measured phenomenon.

Phase-modulated sensors compare the phase of light in a sensing signal to a reference signal in a device known as an interferometer. The interferometers measure the phase difference between both signals with extreme sensitivity. These are much more accurate than intensity-modulated sensors and present a more extensive dynamic range.

Wavelength-modulated sensors work from a change of the transmission or reflection spectrum associated with displacement, temperature, or the presence of chemical species.

Scattering-based sensors are related to three types of light scattering: Rayleigh, Raman, and Brillouin. These sensors detect anomalies along the fiber by changes in the scattered light back-reflected to a detector. The scattered light perturbation may cause an intensity change or wavelength shift caused by the sensed parameter.

Polarization-based sensors modify the polarization state through phenomena such as Faraday rotation or birefringence, which alters the transmitted light intensity [6].

This work will focus on a specific phase-modulated sensor, the Fiber Fabry-Pérot Sensor (FFPI). Due to their extreme sensitivity, phase-modulated sensors are the most publicized fiber sensors [7]. Typically, they involve optical interferometers to measure the phase change of a single light signal or, more often, the relative phase change between two light waves. Interferometer-based fiber optic sensors have been implemented in various applications since 1983 [8]. However, the first published fiber-optic Fabry-Pérot sensing system was registered in 1988 as a high-resolution relative point temperature system [9]. However, the Fabry-Pérot interferometer (FPI) was invented by the physcicist Charles Fabry and Alfred Pérot who published their most significant article in 1897 [10].

The configuration of a conventional FFPI involves single or multiple cavities to generate interference from successive reflections of an initial beam. The Fabry-Pérot fiber cavities can be made using fiber Bragg gratings (FBG) [11], coreless fibers (CF) [12], external mirrors [13], polymers [14], and more. We obtained all the outstanding experimental results presented in this work by interferometers based on a double cavity configuration formed with a polymer cavity and an air cavity using an external mirror. The use of polymers for cavity

formation began in 1996 with an ultrasound FFPI sensor using a thin transparent polymer PET film [15]. A brief timeline diagram of the fiber Fabry-Pérot interferometers is presented in Fig. 1.

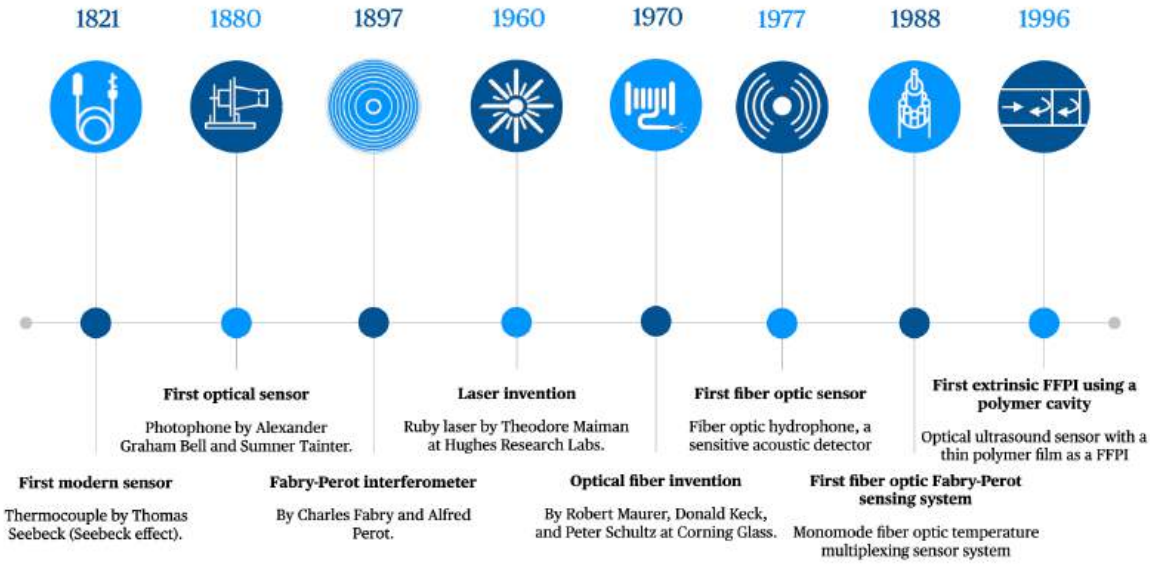

Fig 1. Brief optical sensors history timeline.

This work will study the phenomenon of optical interference in optical fiber sensors, particularly the Fabry-Perot interferometer. The structure of this interferometer is interesting because it is compact, easy to manufacture, and highly sensitive. To improve the sensitivity of these interferometers to the influence of external disturbances, we propose to use a polymer layer adhered to the tip of the optical fiber. The main objective is to demonstrate that the sensitivity and resolution of the reported schemes for measuring distance and temperature can be improved.

In the following chapters, I will present the basis of displacement and temperature sensors, based on a modified extrinsic Fabry Perot interferometer, by adding a semi-spherical polymer cap to the end face of an SMF FC/PC connector, considering its configuration, operation, fabrication, mathematical theory, experimental results, and a mechatronic platform that automates its fabrication process to obtain reproducible devices.

CHAPTER 2:
THEORETICAL MODEL

The characteristics of the light propagating in an SMF can be determined after solving the Helmholtz equation in a cylindrical coordinate system. The solution is a family of Bessel functions (Bessel functions for the core and modified Bessel functions for the cladding). It is helpful to compare the Bessel beam with the Gaussian beam. Whereas the complex amplitude of the Bessel beam is an exact solution of the Helmholtz equation, the complex amplitude of the Gaussian beam is only an approximate solution. The development of the theory presented in this chapter is based on the presented in reference [16].

A single component of $\vec{E}$ or $\vec{H}$ of an electromagnetic wave, represented as ψ, propagating in a uniform medium satisfies the **Helmholtz wave equation**:

$$(\nabla^2 + k^2)\,\psi = 0 \tag{1}$$

where $k = 2\pi/\lambda$ is the wave number, which can also be expressed in terms of the angular frequency ω, the vacuum speed of light c, the relative permittivity ϵ_r, and permeability μ_r of the medium:

$$k = \frac{\omega\sqrt{\epsilon_r \mu_r}}{c} \tag{2}$$

Considering the positive z direction as the direction of propagation, the distribution for any component of the electric field is $E(x, y, z) = u(x, y, z)e^{-jkz}$, where u is a complex scalar function that defines the non-plane wave part of the beam. Thus, substituting the electric field in the Helmholtz equation, we obtain the **reduced wave equation**:

$$\frac{\partial^2 E}{\partial x^2} + \frac{\partial^2 E}{\partial y^2} + \frac{\partial^2 E}{\partial z^2} + k^2 E = 0$$

$$\frac{\partial^2 u}{\partial x^2} + \frac{\partial^2 u}{\partial y^2} + \frac{\partial^2 u}{\partial z^2} - 2jk\frac{\partial u}{\partial z} = 0 \tag{3}$$

Since the variation of the amplitude u along z is small over a distance comparable to a wavelength due to diffraction, this implies $\left[\frac{\Delta\left(\frac{\partial u}{\partial z}\right)}{\Delta z}\right]\lambda << \frac{\partial u}{\partial z}$. In addition, the axial variation is small compared to the perpendicular variation, which means that the third term in (3) is negligible compared to the first two terms. This statements constitute the **paraxial wave equation**, which is presented in the following expression in rectangular coordinates:

$$\frac{\partial^2 u}{\partial x^2} + \frac{\partial^2 u}{\partial y^2} - 2jk\frac{\partial u}{\partial z} = 0 \tag{4}$$

The solutions to the paraxial wave equation are the Gaussian beam modes. The limit condition for the application of considering the paraxial approximation is that the angular divergence of the beam must be confined to within 0.5 radian or about 30 degrees.

The axial symmetry existent in optical fibers makes cylindrical coordinates the natural choice for the solution of the paraxial wave equation, which is in this coordinate system:

$$\frac{\partial^2 u}{\partial r^2}+\frac{1}{r}\frac{\partial u}{\partial r}+\frac{1}{r}\frac{\partial^2 u}{\partial \varphi^2}-2jk\frac{\partial u}{\partial z}=0 \tag{5}$$

where $u \equiv u(r,\varphi,z)$. The axial symmetry implies that u is independent of φ, which makes the third term in equation (5) equal to zero, thus we obtain the **axial symmetric paraxial wave equation**:

$$\frac{\partial^2 u}{\partial r^2}+\frac{1}{r}\frac{\partial u}{\partial r}-2jk\frac{\partial u}{\partial z}=0 \tag{6}$$

The simplest solution of the axial symmetric paraxial equation can be written in the form:

$$u(r,z)=A(z)e^{-\frac{jkr^2}{2q(z)}} \tag{7}$$

where A and q are two complex functions, only dependent on z. In order to obtain both terms, we substitute (7) into (6) obtaining:

$$-2jk\left(\frac{A}{q}+\frac{\partial A}{\partial z}\right)+\frac{Ak^2r^2}{q^2}\left(\frac{\partial q}{\partial z}-1\right)=0 \tag{8}$$

Solving Equation (6)

From (6):

$$\frac{\partial^2 u}{\partial r^2}+\frac{1}{r}\frac{\partial u}{\partial r}-2jk\frac{\partial u}{\partial z}=0$$

We substitute (7) and develop:

$$\frac{\partial^2}{\partial r^2}\left[A(z)e^{-\frac{jkr^2}{2q(z)}}\right]+\frac{1}{r}\frac{\partial}{\partial r}\left[A(z)e^{-\frac{jkr^2}{2q(z)}}\right]-2jk\frac{\partial}{\partial z}\left[A(z)e^{-\frac{jkr^2}{2q(z)}}\right]=0$$

$$-\frac{Ajk}{q}e^{-\frac{jkr^2}{2q}}-\frac{Ak^2r^2}{q^2}e^{-\frac{jkr^2}{2q}}-\frac{Ajk}{q}e^{-\frac{jkr^2}{2q}}-2jk\frac{\partial A}{\partial z}e^{-\frac{jkr^2}{2q}}+\frac{Ak^2r^2}{q^2}\frac{\partial q}{\partial z}e^{-\frac{jkr^2}{2q}}=0$$

$$-\frac{2Ajk}{q}-2jk\frac{\partial A}{\partial z}-\frac{Ak^2r^2}{q^2}+\frac{Ak^2r^2}{q^2}\frac{\partial q}{\partial z}=0$$

$$-2jk\left(\frac{A}{q}+\frac{\partial A}{\partial z}\right)+\frac{Ak^2r^2}{q^2}\left(\frac{\partial q}{\partial z}-1\right)=0$$

Equation (8) must be satisfied for all r and z values. The two parts of the equation must be equal to zero individually to obtain the following two relations that must be simultaneously satisfied:

$$\frac{\partial q}{\partial z} = 1 \tag{9}$$

$$\frac{\partial A}{\partial z} = -\frac{A}{q} \tag{10}$$

Where the solution for (9) is

$$q(z) = q(z_0) + (z - z_0) \tag{11}$$

Considering $z_0 = 0$ as the reference position along the z axis, (11) reduces to

$$q(z) = q(0) + z \tag{12}$$

The function q is known as **complex beam parameter**, **beam parameter** or **Gaussian beam parameter**. Since it appears in (7) as $1/q$ and it is a complex function, can also be represented as

$$\frac{1}{q} = \left(\frac{1}{q}\right)_r - j\left(\frac{1}{q}\right)_i \tag{13}$$

where r and i reference the real and imaginary parts of $1/q$, respectively. Substituting into (7), the exponential term becomes

$$e^{-\frac{jkr^2}{2q(z)}} = e^{\left[\left(-\frac{jkr^2}{2}\right)\left(\frac{1}{q}\right)_r - \left(\frac{kr^2}{2}\right)\left(\frac{1}{q}\right)_i\right]} \tag{14}$$

The imaginary term of (14) has the form of $\phi(r)$ the phase variation relative to a plane for a fixed value of z as function of r, produced by a spherical wavefront in the paraxial limit. In the limit $r \ll R$, and considering $k = 2\pi/\lambda$, the phase delay is approximately:

$$\phi(r) \cong \frac{\pi r^2}{\lambda R} = \frac{kr^2}{2R} \tag{15}$$

Then, from (14) the real part of $1/q$ is the radius of curvature R in the form:

$$\left(\frac{1}{q}\right)_r = \frac{1}{R} \tag{16}$$

The real term of (14) has a Gaussian variation as a function of the distance from the propagation axis. The standard form for a Gaussian distribution is:

$$\left(\frac{1}{q}\right)_i = \frac{2}{kw^2(z)} = \frac{\lambda}{\pi w^2} \tag{17}$$

where w is the **beam radius**, which is the value of the radius at which the field falls to $1/e$ relative to its on-axis value. Thus, the function q is given by

$$f(r) = f(0)e^{\left(\frac{r}{r_0}\right)^2} \tag{18}$$

where r_0 represents the distance to the $1/e$ point relative to the on-axis value. Thus, the mathematical expression for $1/q$ is:

$$\frac{1}{q} = \frac{1}{R} - \frac{j\lambda}{\pi w^2} \tag{19}$$

where both R and w are functions of z. At $z = 0$ we have from (7), $u(r,0) = A(0)e^{-\frac{jkr^2}{2q(0)}}$, and we define $w_0 = \left(\frac{\lambda q(0)}{j\pi}\right)^{1/2}$ as the beam radius at $z = 0$, named as the **beam waist radius**. From (12) we obtain a second important expression for q:

$$q = \frac{j\pi w_0^2}{\lambda} + z \tag{20}$$

From (19) and (20) we obtain the radius of curvature and the beam radius as a function of position along the axis of propagation:

$$R = z + \frac{1}{z}\left(\frac{\pi w_0^2}{\lambda}\right)^2 \tag{21}$$

$$w = w_0\left[1 + \left(\frac{\lambda z}{\pi w_0^2}\right)^2\right]^{1/2} \tag{22}$$

The quantity $\pi w_0^2/\lambda$ is called the **confocal distance**.

Solving Equation (19)

Dividing 1 by (20)

$$\frac{1}{q} = \frac{1}{z + j\frac{\pi w_0^2}{\lambda}}$$

Now multiplying right side of the previous equation by $\left(\frac{z-j\frac{\pi w_0^2}{\lambda}}{z-j\frac{\pi w_0^2}{\lambda}}\right)$:

$$\frac{1}{q}=\frac{z}{z^2+\left(\frac{\pi w_0^2}{\lambda}\right)^2}-j\frac{\frac{\pi w_0^2}{\lambda}}{z^2+\left(\frac{\pi w_0^2}{\lambda}\right)^2}$$

Equalizing its real term with the real term of (19) we obtain:

$$R=z+\frac{1}{z}\left(\frac{\pi w_0^2}{\lambda}\right)^2$$

Equalizing its imaginary term with the imaginary term of (19) we obtain:

$$\frac{\pi w^2}{\lambda}=\frac{z^2+\left(\frac{\pi w_0^2}{\lambda}\right)^2}{\frac{\pi w_0^2}{\lambda}}$$

$$w^2=\frac{\lambda^2 z^2}{\pi^2 w_0^2}+w_0^2$$

$$=w_0^2\left[1+\left(\frac{\lambda z}{\pi w_0^2}\right)^2\right]$$

$$w=w_0\left[1+\left(\frac{\lambda z}{\pi w_0^2}\right)^2\right]^{1/2}$$

From Equation (10), we find $dA/A=-dz/q$, and from (9) $dz=dq$, so that we can write $dA/A=-dq/q$. Hence, $A(z)/A(0)=q(0)/q(z)$, and substituting q from (20), we find:

$$\frac{A(z)}{A(0)}=\frac{1+\frac{j\lambda z}{\pi w_0^2}}{1+\left(\frac{\lambda z}{\pi w_0^2}\right)^2} \qquad (23)$$

Solving Equation (9) and (10)

$$\int \frac{dA}{A} = -\int \frac{dq}{q}$$

$$LnA(z) - LnA(0) = -[Lnq(z) - Lnq(0)]$$

$$\frac{A(z)}{A(0)} = \frac{q(0)}{q(z)}$$

Substituting (20):

$$\frac{A(z)}{A(0)} = \frac{\frac{j\pi w_0^2}{\lambda}}{\frac{j\pi w_0^2}{\lambda} + z}$$

Multiplying by $\frac{z-\frac{j\pi w_0^2}{\lambda}}{z-\frac{j\pi w_0^2}{\lambda}}$ and then by $\frac{\frac{1}{\left(\frac{\pi w_0^2}{\lambda}\right)^2}}{\frac{1}{\left(\frac{\pi w_0^2}{\lambda}\right)^2}}$ we obtain:

$$\frac{A(z)}{A(0)} = \frac{1 + \frac{j\lambda z}{\pi w_0^2}}{1 + \left(\frac{\lambda z}{\pi w_0^2}\right)^2}$$

It is convenient to express the quantity $\frac{\lambda z}{\pi w_0^2}$ in terms of a phasor, so we define:

$$tan\,\phi_0 = \frac{j\lambda z}{\pi w_0^2} \tag{24}$$

Equation (23) becomes:

$$\frac{A(z)}{A(0)} = \frac{w_0}{w} e^{j\phi_0} \tag{25}$$

Solving Equation (23)

From (24)

$$\frac{sin\,\phi_0}{cos\,\phi_0} = \frac{\lambda z}{\pi w_0^2}$$

$$\frac{1 - cos^2\,\phi_0}{cos^2\,\phi_0} = \left(\frac{\lambda z}{\pi w_0^2}\right)^2$$

$$cos^2\,\phi_0 \left[\left(\frac{\lambda z}{\pi w_0^2}\right)^2 + 1\right] = 1$$

$$\cos\phi_0 = \left[\left(\frac{\lambda z}{\pi w_0^2}\right)^2 + 1\right]^{-1/2}$$

$$\cos\phi_0 = \frac{w_0}{w}$$

Substituting into (23) and using (22):

$$\frac{A(z)}{A(0)} = \frac{1 + \mathrm{j}\tan\phi_0}{1 + \tan^2\phi_0}$$

$$= \frac{1 + \mathrm{j}\tan\phi_0}{\sec^2\phi_0}$$

$$= \left(1 + j\frac{\sin\phi_0}{\cos\phi_0}\right)\cos^2\phi_0$$

$$= \cos\phi_0\,(\cos\phi_0 + j\sin\phi_0)$$

$$= \cos\phi_0\, e^{j\phi_0}$$

$$= \frac{w_0}{w} e^{j\phi_0}$$

The term ϕ_0 is known as the Gaussian beam phase shift. If we take the amplitude on-axis at the beam waist to be unity, we obtain the complete expression for the fundamental Gaussian beam mode:

$$u(r,z) = A(0)\frac{w_0}{w} e^{-\frac{r^2}{w^2} - \frac{j\pi r^2}{\lambda R} + j\phi_0} \tag{26}$$

Solving Equation (7)

From (7) we know

$$u(r,z) = A(z)e^{-\frac{jkr^2}{2q(z)}}$$

Substituting (19):

$$u(r,z) = A(z)e^{-\frac{-jkr^2}{2R} - \frac{-k\lambda r^2}{2\pi w^2}}$$

Substituting (25):

$$u(r,z) = A(0)\frac{w_0}{w} e^{-\frac{r^2}{w^2} - \frac{j\pi r^2}{\lambda R} + j\phi_0}$$

Since $E(x,y,z) = u(x,y,z)e^{-jkz}$, we find the expression for the electric field:

$$E(r,z) = A(0)\frac{w_0}{w} e^{-\frac{r^2}{w^2} - jkz - \frac{j\pi r^2}{\lambda R} + j\phi_0} \tag{27}$$

We assume that the electric and magnetic field components are related to each other like those in a plane wave. Thus, the total power is proportional to the square of the electric field

integrated over the area of the beam. The normalized electric field distribution at any distance along the axis of propagation of the fundamental Gaussian beam mode is given by:

$$E(r,z) = \sqrt{\frac{2}{\pi w^2}} e^{-\frac{r^2}{w^2} - jkz - \frac{j\pi r^2}{\lambda R} + j\phi_0} \tag{28}$$

Solving Equation (27)

Starting from the normalization expression:

$$\int_0^\infty |E|^2 \, 2\pi r dr = 1$$

$$\int_0^\infty E \cdot E * 2\pi r dr = 1$$

$$A^2(0)\frac{w_0^2}{w^2} 2\pi \int_0^\infty e^{-\frac{2r^2}{w^2}} r dr = 1$$

$$-A^2(0)\frac{\pi w_0^2}{2} e^{-\frac{2r^2}{w^2}}\Big|_0^\infty = 1$$

$$A(0) = \sqrt{\frac{2}{\pi w_0^2}}$$

Substituting $A(0)$ in (27):

$$\sqrt{\frac{2}{\pi w_0^2}} \frac{w_0}{w} = \sqrt{\frac{2}{\pi w^2}}$$

The **field coupling coefficient** between two Gaussian beams, a and b, is defined as the integral of the complex conjugate of the electric field distribution of the first beam multiplied by the field distribution of the second beam:

$$c_{ab} = \int\int E_a^* \, E_b dS \tag{29}$$

Since we are not going to consider the overall phase shift, we can omit the plane wave shifts:

$$c_{ab} = \int\int u_a^* \, u_b dS \tag{30}$$

If we consider a coupling coefficient in one dimension, we denote (30) as:

$$c_{ab}^{1x} = \int u_a^*(x) u_b(x) dx \tag{31}$$

The two-dimensional field coupling coefficient is the product of the field coupling coefficient for two orthogonal coordinates:

$$c_{ab}^{2} = c_{ab}^{1x} \cdot c_{ab}^{1y} \tag{32}$$

The **power coupling coefficient** between the two beams represents the factor of the incident power flowing in the first beam that ends up in the second. It is the square magnitude of the two-dimensional field coupling coefficient:

$$K_{ab} = |c_{ab}^{2}|^{2} = |c_{ab}^{1x}|^{2} \cdot \left|c_{ab}^{1y}\right|^{2} \tag{33}$$

In the case of a fundamental mode in one dimension, neglecting the overall phase term for the fundamental Gaussian beam mode, (26) becomes:

$$u(x) = \left(\frac{2}{\pi w_x^2}\right)^{1/4} e^{-j\frac{kx^2}{2q_x}} \tag{34}$$

where q_x is the complex beam parameter in one dimension. We obtain for the coupling integral:

$$c_{ax}^{1} = \left(\frac{2}{\pi w_{xa} w_{xb}}\right)^{1/2} \int_{-\infty}^{+\infty} e^{\left(\frac{jkx^2}{2}\right)\left(\frac{1}{q_{xa}^{*}} - \frac{1}{q_{xb}}\right)} dx \tag{35}$$

Where ax denotes an axially aligned beam and the superscript 1 indicates a one-dimensional coupling coefficient. Using $\int_{-\infty}^{\infty} e^{-ax^2+bx}\, dx = \left(\frac{\pi}{a}\right)^{1/2} e^{\frac{b^2}{4a}}$ with $a > 0$, (35) can be evaluated giving us:

$$c_{ax}^{1} = \left[\frac{2j\lambda}{\pi w_{xa} w_{xb}\left(\frac{1}{q_{xa}^{*}} - \frac{1}{q_{xb}}\right)}\right]^{1/2} \tag{36}$$

Considering a symmetric beam, (36) is just squared giving:

$$c_{ax}^{2} = \frac{2j\lambda}{\pi w_a w_b\left(\frac{1}{q_a^{*}} - \frac{1}{q_b}\right)} \tag{37}$$

We consider a reference plane as shown in Fig. 2, where two beams have beam radius w_a and w_b, and radius of curvature R_a and R_b, respectively. The plane is defined by its distance z_a from the plane in which the waist of the first beam has radius w_{0a}, and distance z_b from the waist of the second beam with waist radius w_{0b}. We define $\Delta\phi$ as the phase difference of each beam relative to its waist:

$$\Delta\phi = \phi_{0b} - \phi_{0a} \tag{38}$$

And Δz as the distance difference of the two beam waists:

$$\Delta z = z_b - z_a \tag{39}$$

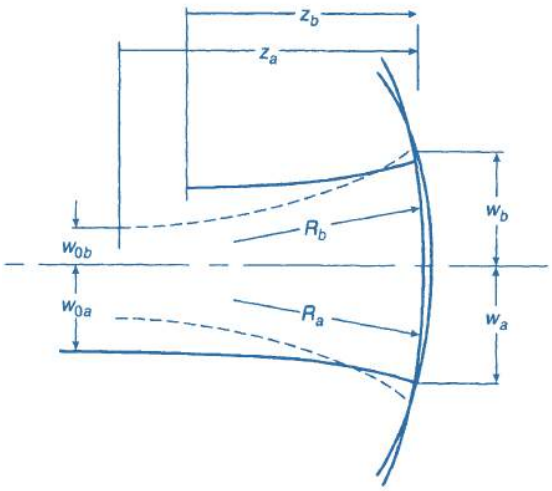

Figure 2. Coupling of two axially aligned Gaussian beams.

Considering phase shifts in (37), we can write:

$$c_{ax}^2 = \frac{2j\lambda e^{j(\Delta\phi - k\Delta z)}}{\pi w_a w_b \left(\frac{1}{q_a^*} - \frac{1}{q_b}\right)} \tag{40}$$

We can express (40) in terms of the beam radius and radius of curvature:

$$c_{ax}^2 = \frac{2e^{j(\Delta\phi - k\Delta z)}}{\left(\frac{w_b}{w_a} + \frac{w_a}{w_b}\right) + j\left(\frac{\pi w_a w_b}{\lambda}\right)\left(\frac{1}{R_a} - \frac{1}{R_b}\right)} \tag{41}$$

Solving Equation (40)

From (19) we know:

$$\frac{1}{q} = \frac{1}{R} - \frac{j\lambda}{\pi w^2}$$
$$= \frac{\pi w^2 - j\lambda R}{R\pi w^2}$$

Substituting in (40)

$$c_{ax}^2 = \frac{2j\lambda e^{j(\Delta\phi - k\Delta z)}}{\pi w_a w_b \left(\frac{\pi w_a^2 + j\lambda R_a}{R_a \pi w_a^2} - \frac{\pi w_b^2 - j\lambda R_b}{R_b \pi w_b^2}\right)}$$

$$= \frac{2j\lambda e^{j(\Delta\phi - k\Delta z)}}{\pi w_a w_b \left(\frac{1}{R_a} - \frac{1}{R_b}\right) + j\lambda\left(\frac{w_b}{w_a} + \frac{w_a}{w_b}\right)}$$

Multiplying by $\frac{\frac{1}{j\lambda}}{\frac{1}{j\lambda}}$

$$= \frac{2j\lambda e^{j(\Delta\phi - k\Delta z)}}{\left(\frac{w_b}{w_a} + \frac{w_a}{w_b}\right) + j\left(\frac{\pi w_a w_b}{\lambda}\right)\left(\frac{1}{R_a} - \frac{1}{R_b}\right)}$$

Equation (41) can be expressed in terms of the parameters of the beam waists from (20):

$$c_{ax}^2 = \frac{2e^{jk\Delta z}}{\left(\frac{w_{0a}}{w_{0b}} + \frac{w_{0b}}{w_{0a}}\right) - \frac{j\lambda\Delta z}{\pi w_{0a} w_{0b}}} \tag{42}$$

Solving Equation (40)

From (40) we have:

$$c_{ax}^2 = \frac{2j\lambda e^{j(\Delta\phi - k\Delta z)} q_a^* q_b}{\pi w_a w_b (q_b - q_a^*)}$$

Using Eq. (20) and Eq. (24) we obtain:

$$\frac{q}{z} = j\frac{1}{tan\,\phi_0} + 1$$

$$q = \frac{z}{sin\,\phi_0}(sin\,\phi_0 + j\,cos\,\phi_0)$$

Substituting in the term $q_a^* q_b$:

$$q_a^* q_b = \frac{z_a z_b}{sin\,\phi_{0a}\,sin\,\phi_{0b}}(sin\,\phi_{0a} - j\,cos\,\phi_{0a})(sin\,\phi_{0b} + j\,cos\,\phi_{0b})$$

$$= \frac{z_a z_b}{sin\,\phi_{0a}\,sin\,\phi_{0b}}[cos(\phi_{0a} - \phi_{0b}) + j\,sin(\phi_{0a} - \phi_{0b})]$$

$$= \frac{z_a z_b}{sin\,\phi_{0a}\,sin\,\phi_{0b}} e^{-j\Delta\phi}$$

Since $sin\,\phi_0 = cos\,\phi_0\,tan\,\phi_0$ and considering $cos\,\phi_0 = \frac{w_0}{w}$ and Eq. (24):

$$sin\,\phi_0 = \frac{\lambda z}{\pi w w_0}$$

Substituting:

$$q_a^* q_b = \frac{\pi^2 w_a w_{0a} w_b w_{0b}}{\lambda^2} e^{-j\Delta\phi}$$

Now the coupling coefficient is:

$$c_{ax}^2 = \frac{j2\pi w_{0a} w_{0b}}{\lambda(q_b - q_a^*)} e^{-jk\Delta z}$$

$$= \frac{j2\pi w_{0a} w_{0b}}{\lambda\left[j\frac{\pi w_{0b}^2}{\lambda} + z_b - \left(-j\frac{\pi w_{0a}^2}{\lambda} + z_a\right)\right]} e^{-jk\Delta z}$$

$$= \frac{j2\pi w_{0a} w_{0b}}{\lambda\Delta z + j\pi(w_{0b}^2 + w_{0a}^2)} e^{-jk\Delta z}$$

Multiplying by $\frac{\frac{j}{\pi w_{0a} w_{0b}}}{\frac{j}{\pi w_{0a} w_{0b}}}$ we obtain:

$$c_{ax}^2 = \frac{2e^{jk\Delta z}}{\left(\frac{w_{0a}}{w_{0b}} + \frac{w_{0b}}{w_{0a}}\right) - \frac{j\lambda\Delta z}{\pi w_{0a} w_{0b}}}$$

The power coupling coefficient is obtained by taking the squared magnitude of the two-dimensional field coupling coefficient:

$$K_{ax} = |c_{ax}^2|^2 = \frac{4}{\left(\frac{w_{0a}}{w_{0b}} + \frac{w_{0b}}{w_{0a}}\right)^2 + \left(\frac{\lambda\Delta z}{\pi w_{0a} w_{0b}}\right)^2} \tag{43}$$

On the other hand, in the paraxial ray-optics approximation, an optical system can be described by a 2x2 ray-transfer matrix M whose elements, $A = M(1,1)$, $B = M(1,2)$, $C = M(2,1)$ and $D = M(2,2)$, are relating to the position and inclination of both the transmitted and the incident ray. This is based on the complex beam parameter method, also known as the ABCD Ray Matrix method, developed by Kogelnik et al. [17].

The similarity between the complex beam parameter q describing a Gaussian beam and the radius of curvature of a geometrical optics beam representation suggests that quasi-optical systems can be analyzed in terms of their effect on q in a manner analogous to the treatment of rays in a linear geometrical optics system. In this approach, the location and slope of a ray at the output plane of a paraxial system are defined to be linear functions of the parameters of the input ray. Denoting the position as r and the slope as r', the linear relation between input and output ray position and slope are:

$$r_{out} = Ar_{in} + Br'_{in} \tag{44}$$

$$r'_{out} = Cr_{in} + Dr'_{in} \tag{45}$$

If we consider (44) and (45) as a column matrix, the effect of the system element can be expressed as:

$$\begin{bmatrix} r_{out} \\ r'_{out} \end{bmatrix} = \begin{bmatrix} A & B \\ C & D \end{bmatrix} \begin{bmatrix} r_{in} \\ r'_{in} \end{bmatrix} \tag{46}$$

Since the radius of curvature is defined by $R = r/r'$, we use (44) and (45) to obtain the expression:

$$R_{out} = \frac{AR_{in} + B}{CR_{in} + D} \tag{47}$$

Solving Equation (46)

Dividing (44) by (45):

$$\frac{r_{out}}{r'_{out}} = \frac{Ar_{in} + Br'_{in}}{Cr_{in} + Dr'_{in}}$$

Multiplying by $\frac{\frac{1}{r'_{in}}}{\frac{1}{r'_{in}}}$ and considering $R = r/r'$:

$$R_{out} = \frac{AR_{in} + B}{CR_{in} + D}.$$

We can relate the complex beam parameter with the radius of curvature by (16), obtaining:

$$q_{out} = \frac{Aq_{in}+B}{Cq_{in}+D}. \tag{48}$$

With the complex beam parameter, we can obtain the beam radius w and the radius of curvature R:

$$w = \left[\frac{\lambda}{\pi\, Im(-1/q)}\right]^{1/2}, \quad R = \left[Re\left(\frac{1}{q}\right)\right]^{-1}. \tag{49}$$

Since E depends on w and R, as seen in (28), the electric field is also modified, which directly affects the coupling of the incident Gaussian beam to the reflected one. For a quasi-optical system, using the transfer matrix, we can calculate the power coupling coefficient:

$$K_{ax} = \eta_{general} = \frac{4z_c^2}{B^2+z_c^2(A^2+D^2+2)+z_c^4C^2} \tag{50}$$

where $z_c = \frac{\pi w_0^2}{\lambda}$ is the confocal distance. (50) applies for any optical system through its general transfer matrix M obtained by multiplying the corresponding ABCD matrices of each one of the n number of optical elements in the form: $M = M_n M_{n-1} M_{n-2} \cdots M_3 M_2 M_1$.

Solving Equation (50)

Considering the first beam is located at the position of zero axial distance ($z = 0$ and $w = w_0$). From (20), the complex beam parameter of the first beam is:

$$q_1 = j\frac{\pi w_0^2}{\lambda} = jz_c$$

Using (48) we can obtain the complex beam parameter of the second beam:

$$\frac{1}{q_2} = \frac{jz_cC + D}{jz_cA + B}$$

Multiplying by the complex conjugate of the denominator and considering that the ABCD matrix parameters satisfy $AD - BC = 1$:

$$\frac{1}{q_2} = \frac{z_c^2AC + BD - jz_c}{z_c^2A^2 + B^2}$$

Now we calculate:

$$\frac{1}{q_1^*} - \frac{1}{q_2} = -\frac{1}{jz_c} - \frac{jz_cC + D}{jz_cA + B}$$
$$= -\frac{jz_c(A + D) + B - z_c^2C}{jz_cB - z_c^2A}$$

From (49), the beam radius of the second beam is:

$$w_2 = \left[\frac{\lambda}{\pi\, Im\left(-\frac{1}{q_2}\right)}\right]^{1/2}$$
$$= \sqrt{\frac{\lambda(A^2z_c^2 + B^2)}{\pi z_c}}$$

The two-dimensional field coupling coefficient from Eq. (40) is:

$$c_{ax}^2 = \frac{2j\lambda}{\pi w_a w_b\left(\frac{1}{q_a^*} - \frac{1}{q_b}\right)}$$
$$= \frac{2j}{\sqrt{A^2z_c^2 + B^2}}\left[\frac{z_c^2A - jz_cB}{jz_c(A + D) + B - z_c^2C}\right]$$

The power coupling coefficient is then:

$$K_{ax} = |c_{ax}^2|^2 = c_{ax}^2 \cdot (c_{ax}^2)^* = \frac{4z_c^2}{B^2 + z_c^2(A^2 + D^2 + 2) + z_c^4 C^2}$$

In this approach tilted beams or offset beams, i.e., misaligned axes beams either in angular or position, are not considered. This analysis applies to any Gaussian beam mode in the paraxial limit. Nevertheless, we are limited to the fundamental mode since the approximation of the Gaussian beam to the Bessel beam only works for the fundamental mode. Furthermore, the equations are valid to any quasi-optical system by just obtaining its overall ABCD matrix from a cascaded representation of its constituent elements [18]. A list of optical components and their matrix transfer values is presented in Table 1.

Finally, the coupling coefficients for a polymer capped optical fiber Fabry-Pérot interferometers (PC-FFPI) can be calculated from the coupling matrices:

$$M_{\eta_1} = M_5 M_4 M_3 M_2 M_1. \tag{51}$$

$$M_{\eta_2} = M'_9 M'_8 M'_7 M'_6 M'_5 M'_4 M'_3 M'_2 M'_1. \tag{52}$$

where $M_1 = \begin{bmatrix} 1 & 0 \\ 0 & \frac{n_{fcore}}{n_{pol}} \end{bmatrix}$, $M_2 = \begin{bmatrix} 1 & L_{pol} \\ 0 & 1 \end{bmatrix}$, $M_3 = \begin{bmatrix} 1 & 0 \\ -\frac{2}{R} & 1 \end{bmatrix}$, $M_4 = M_2$, $M_5 = \begin{bmatrix} 1 & 0 \\ 0 & \frac{n_{pol}}{n_{fcore}} \end{bmatrix}$, $M'_1 = \begin{bmatrix} 1 & 0 \\ 0 & \frac{n_{fcore}}{n_{pol}} \end{bmatrix}$, $M'_2 = M_2$, $M'_3 = \begin{bmatrix} 1 & 0 \\ \frac{n_{air} - n_{pol}}{n_{air} R} & \frac{n_{pol}}{n_{air}} \end{bmatrix}$, $M'_4 = \begin{bmatrix} 1 & L_{air} \\ 0 & 1 \end{bmatrix}$, $M'_5 = \begin{bmatrix} 1 & 0 \\ 0 & 1 \end{bmatrix}$, $M'_6 = M_2$, $M'_7 = \begin{bmatrix} 1 & 0 \\ \frac{n_{air} - n_{pol}}{n_{pol} R} & \frac{n_{air}}{n_{pol}} \end{bmatrix}$, $M'_8 = M'_4$, and $M'_9 = \begin{bmatrix} 1 & 0 \\ 0 & \frac{n_{pol}}{n_{fcore}} \end{bmatrix}$.

With n_{fcore} as the refractive index of the fiber optic core, n_{pol} is the polymer refractive index, n_{air} is the air refractive index, L_{air} is the physical air cavity length, and L_{pol} is the physical polymer length. (51) presents five matrices due to the round trip of light across five optical elements: refraction at a planar boundary (n_{fcore} to n_{pol}), free space propagation (polymer), reflection from a spherical mirror, free space propagation (polymer), and refraction at a planar boundary (n_{pol} to n_{fcore}). (52) presents nine matrices due to the round trip of light across nine optical elements: refraction at a planar boundary (n_{fcore} to n_{pol}), free space propagation (polymer), refraction at a spherical boundary, free space propagation (air), reflection from a spherical mirror, free space propagation (air), refraction at a spherical boundary, free space propagation (polymer), and refraction at a planar boundary (n_{pol} to n_{fcore}). In this interferometer, due to the large length of the dual cavity and the spherical shape of the polymer cavity that affects the intensity of the light recoupled in the core of the SMF after traveling through the polymer and air cavities, the calculus of the coupling coefficient η_2 is very relevant to evaluate the intensity of the interference pattern more accurately.

	A	B	C	D
Free-space propagation.	1	L	0	1
Reflection at a planar boundary.	1	0	0	$\frac{n_1}{n_2}$
Refraction at a spherical boundary (Convex: R>0; concave: R<0).	1	0	$-\frac{n_2 - n_1}{n_2 R}$	$\frac{n_1}{n_2}$
Transmission through a thin lens (Convex: f>0; concave: f<0).	1	0	$-\frac{1}{f}$	1
A thin lens of material with index n_2, embedded in material of index n_1. With radius of curvature of the first surface R_2 and second surface R_1.	1	0	$\frac{n_2 - n_1}{n_1}\left(\frac{1}{R_1} - \frac{1}{R_2}\right)$	1
Reflection from a spherical mirror (Convex: R>0; concave: R<0).	1	0	$-\frac{2}{R}$	1
Reflection from an ellipsoidal mirror with d_1 and d_2 the distances from the center to the respective foci.	1	0	$-\left(\frac{1}{d_1} + \frac{1}{d_2}\right)$	1
Reflection from a planar mirror.	1	0	0	1

Table 1. Ray transformation matrices.

The general equation that describes the intensity I_{FFPI} of a single-cavity FFPI [19] is given by

$$I_{FFPI} = I_1 + I_2 + 2\sqrt{I_1 I_2}\cos\phi \tag{53}$$

where

$$\phi = \frac{2\pi}{\lambda} 2OPL \tag{54}$$

OPL is the optical path length. Equation (53) is usually represented in terms of the reflectance R and the transmittance T, which both can be obtained by the Fresnel reflection r and transmission t coefficients for an interface with two different refractive indexes n_1 and n_2:

$$r = \frac{n_2 - n_1}{n_1 + n_2} \tag{55}$$

$$t = \frac{2n_1}{n_1 + n_2} \tag{56}$$

On the other hand, both coefficients are also defined in terms of the incident E_0, the reflected E_r, and the transmitted field E_t:

$$r = \frac{E_r}{E_0} \tag{57}$$

$$t = \frac{E_t}{E_0} \tag{58}$$

Considering the conditions $r = -r'$ and $rr' = r^2$, we can represent them in terms of the incident I_0, the reflected I_r, and the transmitted irradiance I_t:

$$r^2 = \frac{I_r}{I_0} \tag{59}$$

$$tt' = \frac{I_t}{I_0} \tag{60}$$

Since we know that $r^2 = R$, $tt' = T$, and $T = 1 - R$, we can obtain the relations:

$$\frac{I_r}{I_0} = R \tag{61}$$

$$\frac{I_t}{I_0} = 1 - R \tag{62}$$

Finally, considering the coupling coefficient $\eta = \frac{I_l}{I_0}$, we can write the intensity I_{FFPI} of a single-cavity FFPI:

$$I_{FFPI} = \left[R_1 + (1 - R_1)^2 R_2 + 2\sqrt{(R_1 R_2)}\eta(1 - R_1)\, cos\left[\frac{2\pi}{\lambda}(2\mathrm{nL})\right]\right] I_0 \tag{63}$$

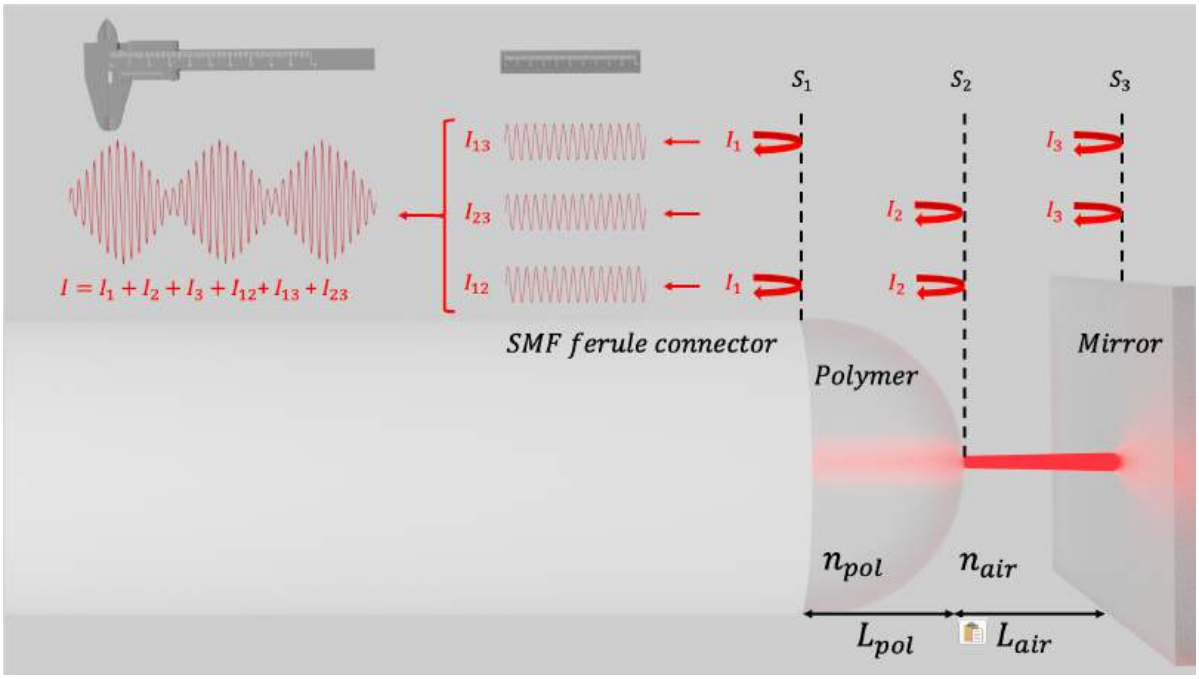

Figure 3. Structure of a double cavity sensor based on a PC-FFPI.

The general equation that describes the intensity I_{DFFPI} of a dual-cavity FFPI is given by

$$I_{DFFPI} = I_1 + I_2 + I_3 + 2\sqrt{I_1 I_2}\, cos\, \phi_{12} + 2\sqrt{I_1 I_3}\, cos\, \phi_{13} + 2\sqrt{I_2 I_3}\, cos\, \phi_{23} \quad (64)$$

The principle of three-beam interference is based on the interference of three reflective surfaces, as presented in Figure 3.

$$I_{PC-FFP} = \Big[R_1 + R_2(1-R_1)^2\eta_1^2 + R_3(1-R_1)^2(1-R_2)^2\eta_2^2 + 2\sqrt{R_1R_2}\eta_1(1-R_1)\cos\Big[\frac{2\pi}{\lambda}\big(2OPL_{pol}\big)\Big] + 2\sqrt{R_1R_3}\eta_2(1-R_1)(1-R_2)\cos\Big[\frac{2\pi}{\lambda}\big(2OPL_{pol} + 2OPL_{air}\big)\Big] + 2\sqrt{R_2R_3}\eta_1\eta_2(1-R_1)^2(1-R_2)\cos\Big[\frac{2\pi}{\lambda}(2OPL_{air})\Big]\Big]\, I_0 \quad (65)$$

Where R_1, R_2, and R_3 represent the reflectance at the surface interfaces S_1, S_2, and S_3, respectively.

CHAPTER 3:
TIPS FABRICATION

Any fabrication process requires a systematic method in order to obtain a reproducible final result. In this Chapter, I present the detailed procedure for the PC-FFPI's fabrication, using SMF connectors. In the Chapter 6, I will present the definitive fabrication process by the implementation of an automatic mechatronic platform.

Besides the SMF FC/PC connectors, I used several bare SMF to fabricate the PC-FFPI. In the first stage of the research, it was necessary to use special equipment, such as the Vytran fusion splicer. In one of the holders I placed an optical fiber whose tip was covered with the polymer (container fiber SMF2), in the other one I placed a cleaned and cleaved optical fiber (receptor fiber SMF1). The Vytran equipment allows to move the fiber holders precisely, so the fiber covered with polymer was moved until the polymer touches the end of the receptor fiber. In order to transfer the most possible quantity of polymer, we move the container fiber transversally around $50\mu m$ and then separate the fiber until it breaks the polymer surface tension. At the fiber tip end, the polymer adopts a semi-spherical or dome shape. The general procedure is represented in Fig. 4 (a)-(f).

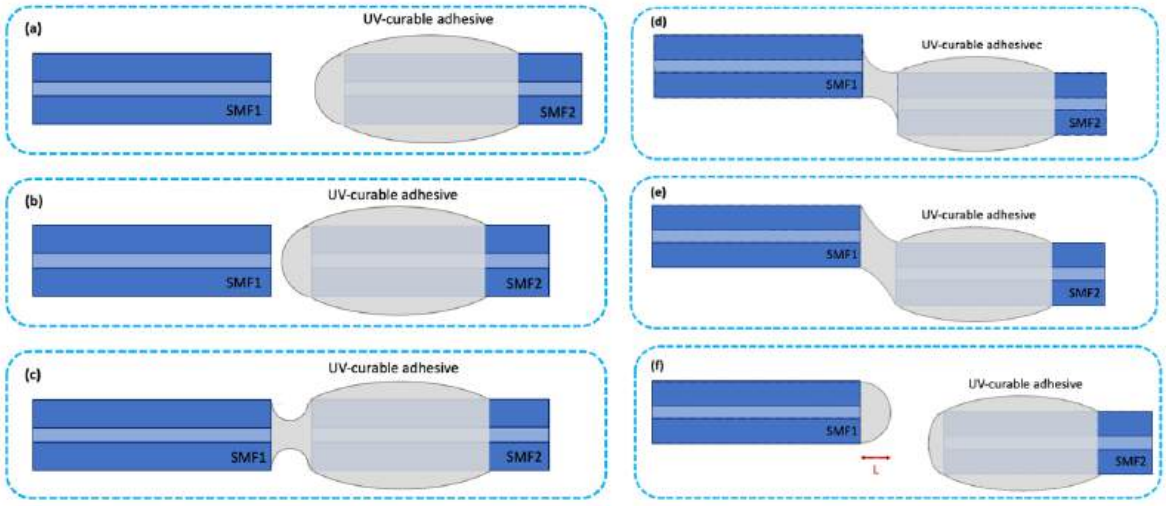

Figure 4. Polymer transferring process to fabricate a SMF tip with a polymer dome shape.

Fig. 5 (a) shows a real picture of the receptor and container fiber before the polymer transfer, taken with the Vytran camera. Then, in Fig. 5 (b), we can observe the final fiber tip with the dome-shaped polymer. This procedure was also used to fabricate tips with tapered fibers to compare the performance of these tips for different cavity lengths according to the fiber type used. Fig. 6 shows a taper with diameter of $\sim 70\mu m$ after the transferring process.

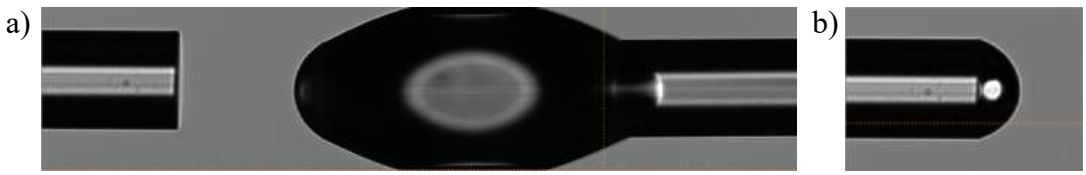

Figure 5. Real picture of the polymer transferring process of a SMF tip (a) before and (b) after the polymer transfer.

Fig. 6. Real picture of the polymer transferring process of a taper tip after the polymer transfer.

The PC-FFPIs were the most used devices in this study. I also fabricated some PC-FFPI using SMF FC/PC connectors using two different types of polymers: polydimethylsiloxane (PDMS) and Norland Optical Adhesive 81 (NOA81), whose refractive index are $n_{PDMS} = 1.39$ [20] and $n_{NOA81} = 1.54$ [21] at 1550 nm, respectively. We prepared PDMS by mixing 10 portions of elastomer and 1 portion of curing agent [22].

The process of attaching the polymer over the end face of the ferrule of the SMF connector was made with an experimental set-up represented in Fig. 7. Due to the large area of the ferrule cross-section, sophisticated cameras or highly precise translation stages are not needed to move the connector. First, I fixed one end of the SMF connector to a translation stage (NRT150/M, Thorlabs), while the other end was connected to the Micronoptics sm125 interrogator. We moved the translation stage until the surface of the ferrule touched the surface of the polymer deposited in a container. After this, I moved the connector slowly away by micrometric displacements, and a portion of the polymer kept adhered to the surface of the ferrule; a step-by-step picture motion of this process is represented in Fig. 8. To know the thickness of the polymer cap during the different stages of the fabrication process, I analyzed the optical spectrum measured with the sm125 interrogator and then calculated the Fourier transform. The peak position in the Fourier spectrum provides the optical path length of the polymer cavity. I did this procedure in real time using an automated program in LabView.

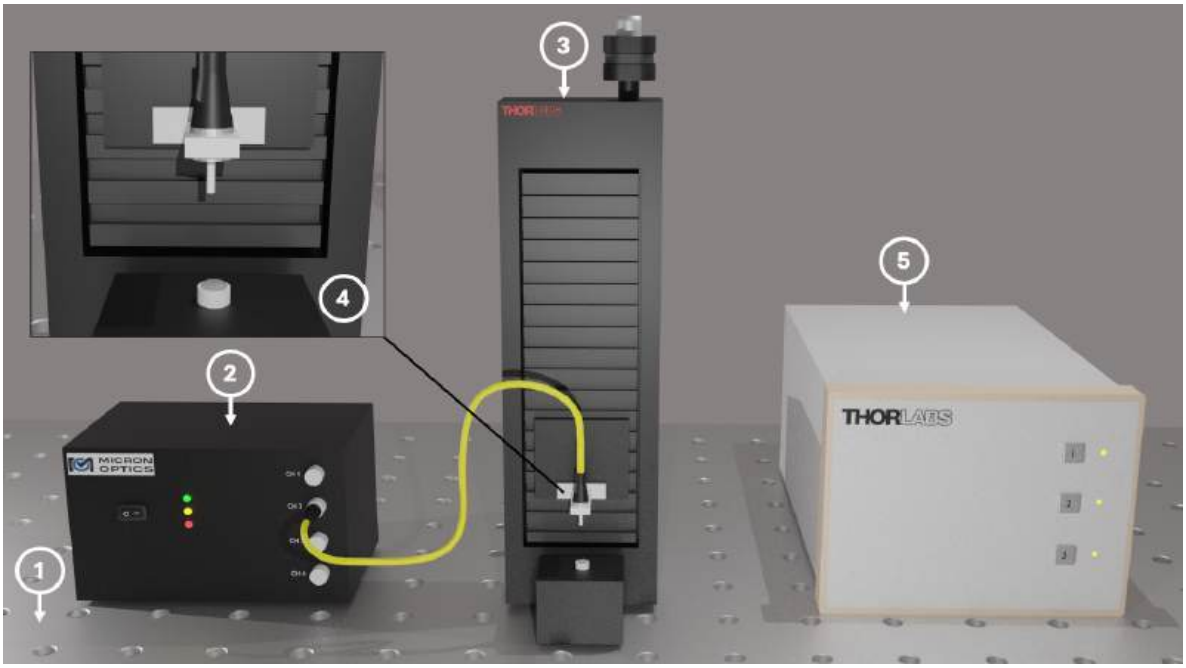

Figure 7. Experimental set-up for ferrule connectors tips fabrication: 1. Optical table. 2. The sm125 interrogator. 3. Motorized translation stage (1-axis). 4. ferrule connector and polymer container. 5. Stepper motor controller.


Figure 8. Real pictures of the polymer transferring process of a ferrule connector tip.

It is possible to reduce the amount of polymer adhered to the surface of the ferrule by touching the polymer surface with the tip of a pin. With this procedure, the original thickness of the polymer cavity decreases by approximately 0.02 mm. Fig. 9 shows this cavity length reduction, which is barely noticeable. Due to the surface tension of the polymer on the face of the connector, each time a polymer portion is removed, it re-forms the shape of the concave surface but with a different radius of curvature.


Figure 9. Real pictures of the tip cavity length reduction.

After the polymer transferring process, the polymer, whether NOA or PDMS, must be cured. In the case of PDMS, we use an experimental set-up like the one presented in Fig. 10; since PDMS solidifies with heat exposure, we heated up the polymer-capped connector at 60°C for 1.5 h using a Peltier plate (Orbital mixing chilling/heating dry bath, Ecotherm). When PDMS is cured, I proceeded to characterize the PC-FFPI fabricated to temperature response.

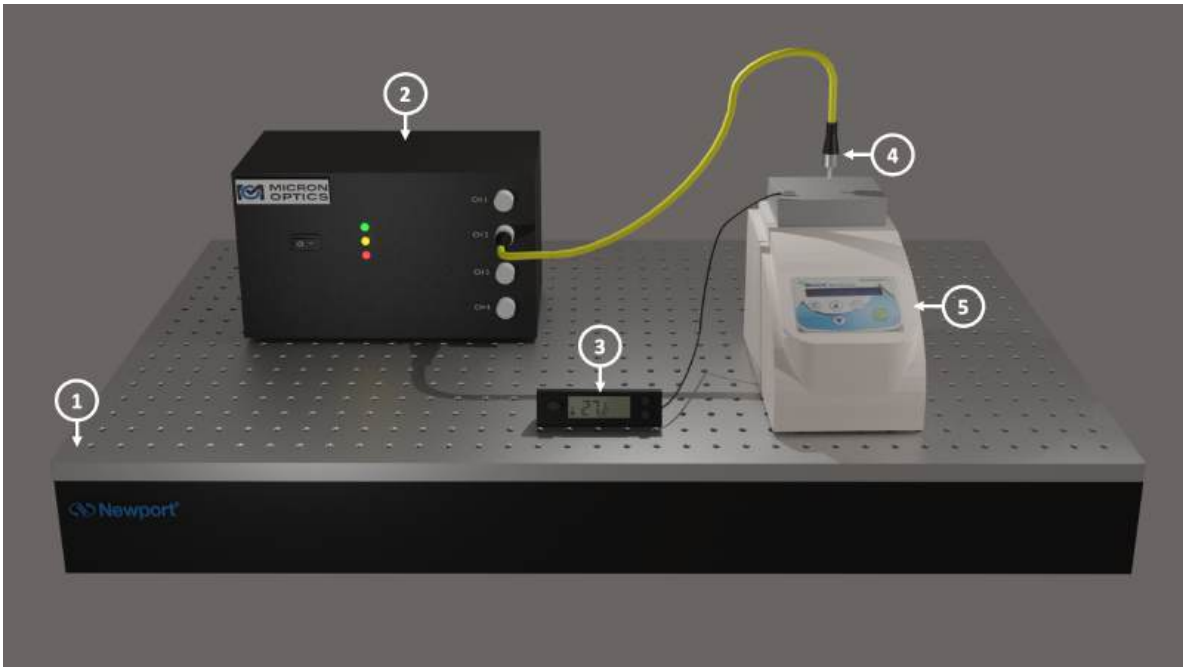

Figure 10. Experimental set-up for the PDMS curing process: 1. Optical table. 2. The sm125 interrogator. 3. Digital thermometer with thermocouple. 4. ferrule connector with a polymer cap. 5. Dry bath with block.

In the case of the PC-FFPI's polymer is NOA81, I cured it with a Norland Opticure LED 200 Light Gun for 15 minutes to solidify the tip and avoid contact deformations. Fig. 11 shows a representation of the experimental set-up used.

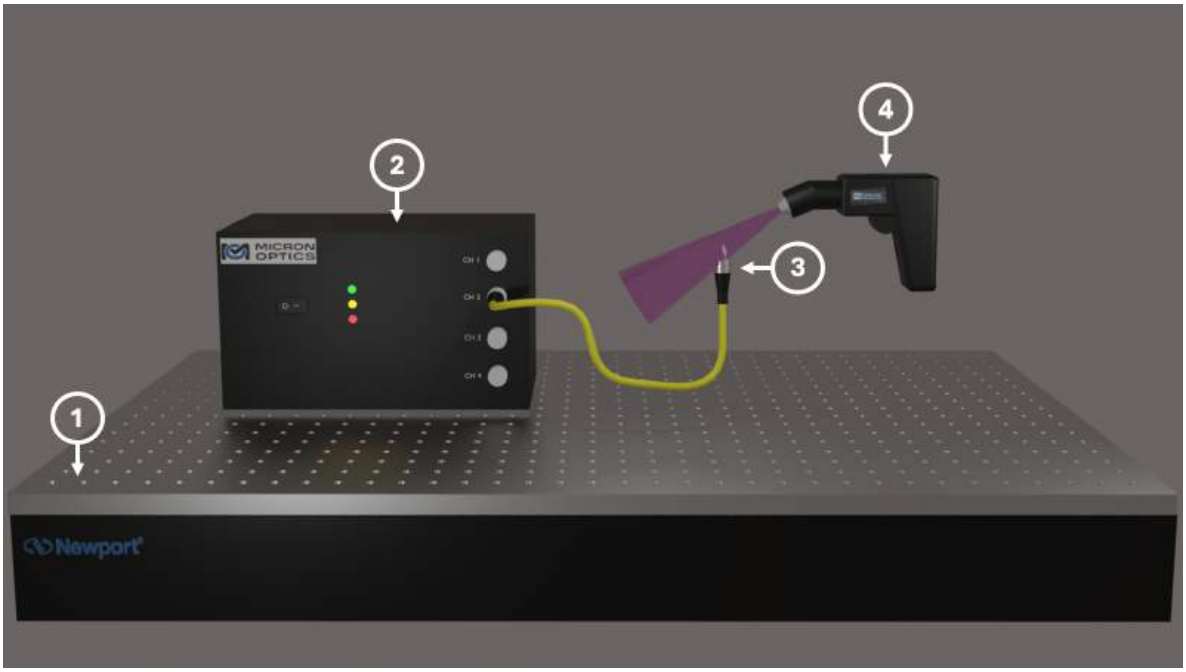

Figure 11. Experimental set-up for the NOA curing process: 1. Optical table. 2. The sm125 interrogator. 3. ferrule connector with a polymer cap. 4. Norland UV light gun.

In the picture of Fig. 12 taken with the Navitar microscope Resolv4K, we can observe the polymer's semi-spherical or dome shape. According to the mathematical theory described in the previous chapter, the radius of curvature plays an essential role in the tip's performance.

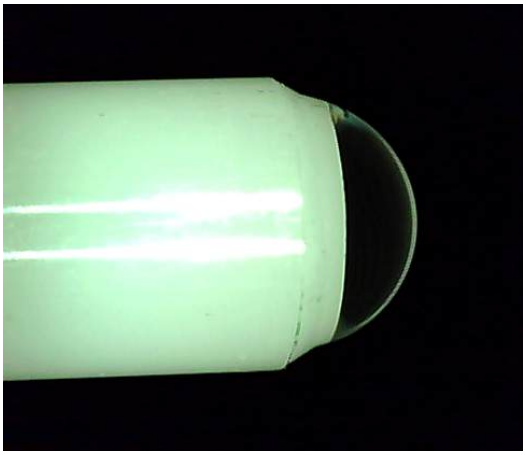
Figure 12. Real picture of the ferrule connector tip with the polymer cap.

The radius of curvature R (Fig. 13) of the polymer cap can be easily calculated in terms of the polymer cavity length L_{pol} and the diameter of the ferrule connector d_c:

$$R = \frac{L_{pol}}{2} + \frac{d_c^2}{8L_{pol}}. \tag{66}$$

Solving equation (66)

Starting from the relations

$$sin\frac{\theta}{2} = \frac{d_c/2}{R}$$

$$d_c = 2R\,sin\frac{\theta}{2}$$

$$d_c^2 = 4R^2\,sin^2\frac{\theta}{2}$$

$$= 4R^2\left(1 - cos^2\frac{\theta}{2}\right)$$

$$cos\frac{\theta}{2} = \sqrt{1 - \frac{d_c^2}{4R^2}}$$

Now it can also be demonstrated that:

$$cos\frac{\theta}{2} = \frac{R-L}{R}$$

$$L = R - R\,cos\frac{\theta}{2}$$

$$= R\left(1 - cos\frac{\theta}{2}\right)$$

Substituting in the relation of $cos\frac{\theta}{2}$ in the previous equation:

$$L = R\left(1 - \sqrt{1 - \frac{d_c^2}{4R^2}}\right)$$

$$\left[\sqrt{1 - \frac{d_c^2}{4R^2}} = 1 - \frac{L}{R}\right]^2$$

$$\left[1 - \frac{d_c^2}{4R^2} = 1 - \frac{2L}{R} + \frac{L^2}{R^2}\right]R^2$$

$$R^2 - \frac{d_c^2}{4} = R^2 - 2LR + L^2$$

$$R = \frac{L^2 + \frac{d_c^2}{4}}{2L}$$

At the end we obtain:

$$R = \frac{L_{pol}}{2} + \frac{d_c^2}{8L_{pol}}.$$

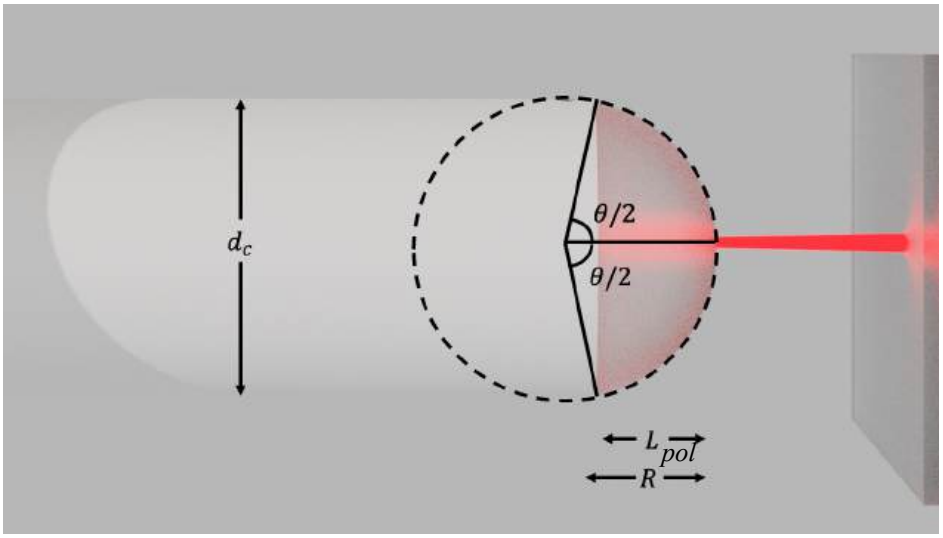

Figure 13. Curvature radius of the polymer cap adhered to the ferrule connector.

Fig. 14(a) and (b) show the image of a pair of devices fabricated with the previously described method. The curvature diameter obtained with processing image software RisingView are $D1$=2.59 mm and $D2$=2.58 mm. The optical and Fourier spectra are shown in Fig. 15 (a) allowing us to determine that $OPL1$ = 0.7217 mm and $OPL2$= 0.7272 mm, respectively. Using (66) and assuming that n_{NOA81}=1.54 a $D1$=2.602 mm and $D2$= 2.588 mm were obtained. A maximum difference of 6 μm between the measured and calculated radius is observed.

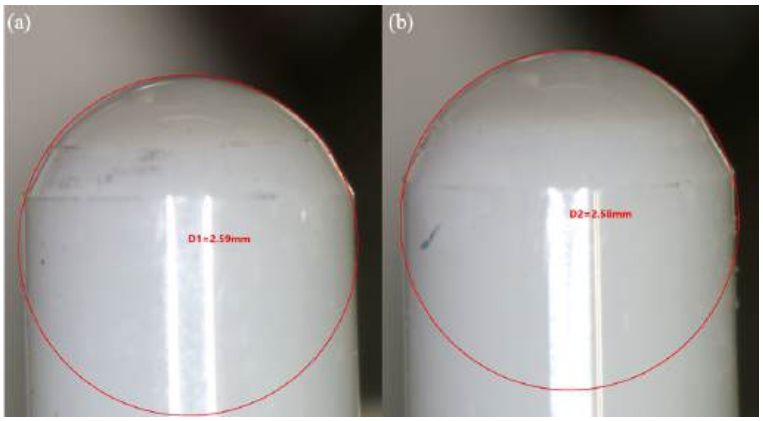

Figure 14. Real pictures of two PC-FFPI fabricated with a similar diameter of curvature (a) 2.59 mm, (b) 2.58 mm.

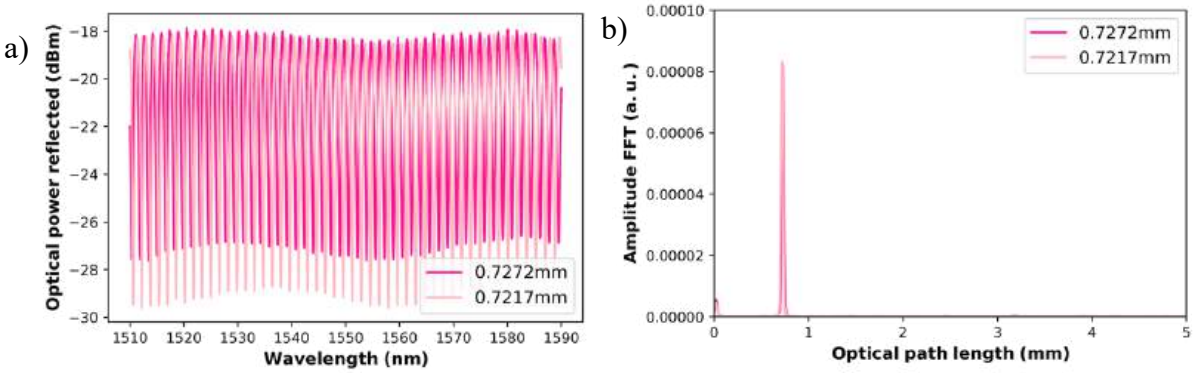

Figure 15. (a) Optical and (b) Fourier domain spectra of the two PC-FFPI fabricated with a similar diameter of curvature, with OPL 0.7272 mm and 0.7217 mm.

We tested one of the PC-FFPIs and compared its Fourier spectra over a time interval of ∼1 month in the same initial position. Both spectra are presented in Fig. 16, where we can observe a bare difference in the amplitude of the three Fourier peaks. However, its optical path lengths remain without modification, which means the cavity length did not suffer any deformation. External factors, such as connection or dirty material issues, could have caused the PC-FFPI's amplitude reduction.

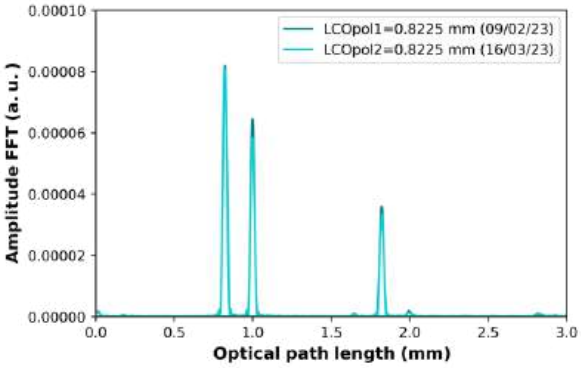

Figure 16. Fourier domain spectra calculated from two optical spectra of a PC-FFPI measured with ∼1 month difference since it was fabricated.

CHAPTER 4: DISPLACEMENT MEASUREMENT

Displacement sensors are a collection of techniques or instruments capable of detecting how much an object has moved and its minimal change in position with high precision, avoiding failures or misreading [23]. Nevertheless, displacement measurement has also been successfully used as an indirect method to detect the occurrence of physical phenomena [24]. Although displacement sensors with good performance based on mechanical or electrical transduction have been developed, optical displacement sensors have gained attention since they have demonstrated the capability to carry out non-contact measurements with ultrahigh sensitivity [25], or due to its capability to monitor displacements in a confined or difficult-to-reach space, for example, inside the body of living beings, through the use of an optical fiber [26].

The extrinsic fiber Fabry-Pérot interferometer (EFPI) is the most popular optical fiber displacement sensor [27], basically due to the simplicity of its structure consisting of a single-mode optical fiber (SMF) tip pointing out to the surface of the object under monitoring. The object's displacement changes the optical path length of the beam propagating along the air gap or cavity. Accordingly, a change in the spectrum of the reflected intensity is produced. Due to the divergence of the light beam when it exits the SMF core, the maximum distance that can be measured with an EFPI is around a centimeter [28]. Over the years, several strategies to reduce or eliminate the divergence of the testing light beam have been successfully demonstrated, for instance, by splicing an SMF tip to a micrometric segment of graded-index multimode fiber [29] or a segment of strongly coupled seven-core fiber [30], attaching an external lens to the SMF tip [28], or using a tapered SMF tip [31]. All these strategies involve using specialized equipment and tools operated by trained personnel.

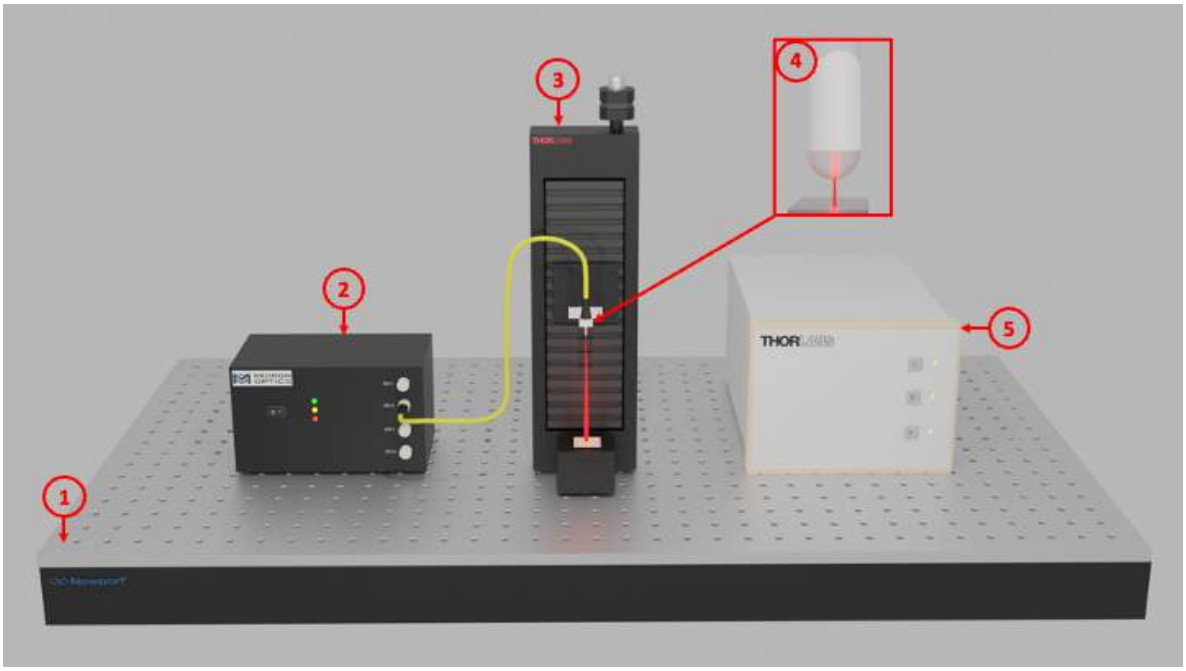

Figure. 17. Experimental set-up for distance characterization: 1. Optical table. 2. The sm125 interrogator. 3. Motorized translation stage (1-axis). 4. ferrule connector with polymer tip and mirror. 5. Stepper motor controller.

The dynamic range of a conventional EFPI displacement sensor is defined as the maximal magnitude that can be measured without significant distortion in the interference pattern. In this case, it is determined by the allowed maximal cavity length.

I implemented a displacement characterization for four different configurations of EFPI using the set-up shown in Fig. 17. First, I used a bare SMF placed in front of a high-reflective mirror, forming an EFPI with a single air cavity. We increased the air cavity from a distance close to zero to a maximum distance where the interference spectrum obtained was readable, i.e., the peak amplitude in the Fourier domain is at least twice higher than the average level of the signal noise amplitude. The optical and Fourier spectra obtained with the bare SMF at different air-cavity lengths are presented in Fig. 18(a) and 18(b), respectively. The peak position in the Fourier domain allowed us to determine the OPL of the air cavity. By tracking the position of the peak of the Fourier spectra at every air cavity length measured, we can plot a displacement characterization curve, as shown in Fig. 18(c). The dynamic range experimentally measured was 10 mm.

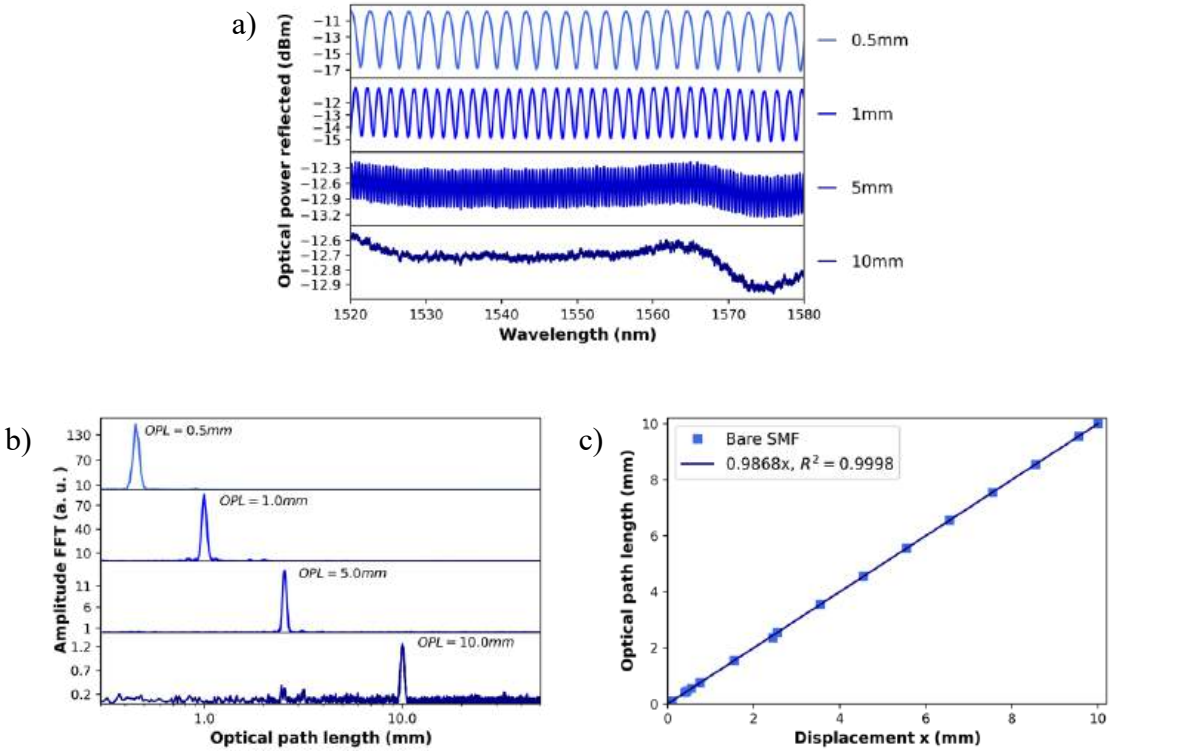

Figure 18. (a) Reflection spectra of single cavity EFPI using a bare SMF, with $OPL_{air} = 0.5, 1, 5, 10$ mm; (b) Fourier spectra for every OPL_{air} measured; (c) corresponding displacement characterization.

Through the same experimental set-up, I characterized a second single cavity EFPI configuration using a $\sim 55\ \mu m$ diameter tapered fiber previously presented in Chapter 3. At this diameter the light is not guided by the core but by the cladding [25]. This device showed a dynamic range of 40 mm, four times larger than that obtained with an untapered bare SMF. The optical and Fourier spectra obtained with the taper at different air-cavity lengths are

presented in Fig. 19(a) and 19(b), respectively. The displacement characterization curve is shown in Fig. 19(c).

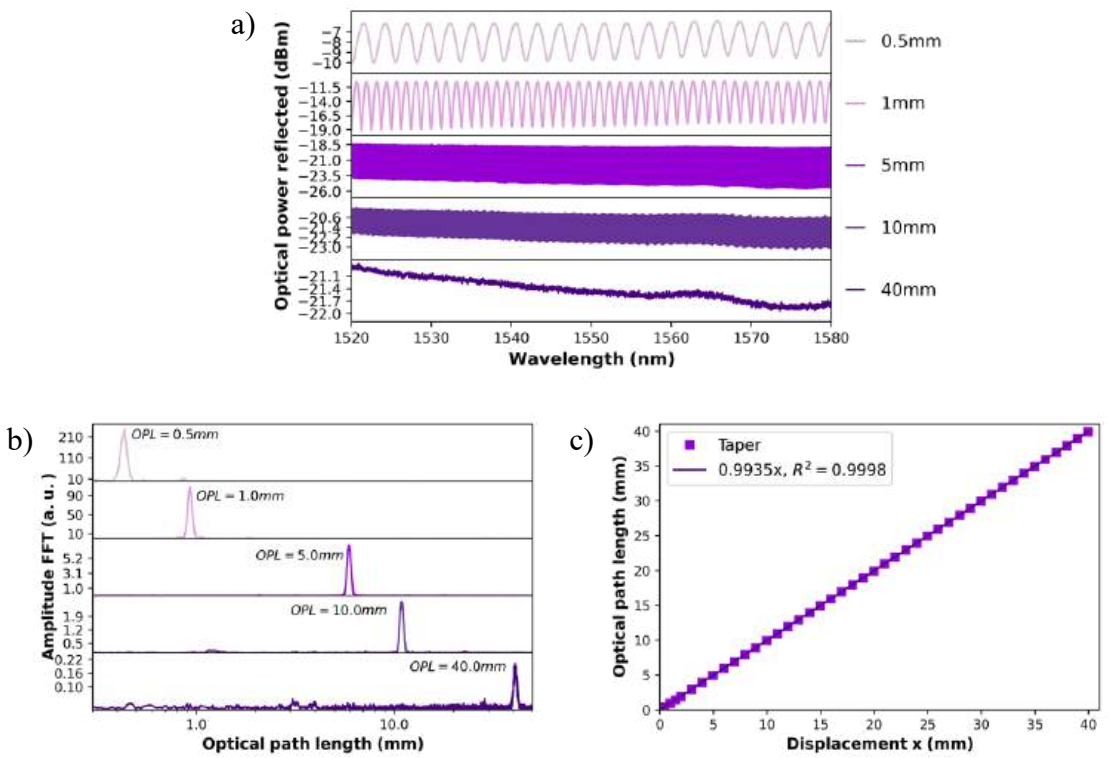

Figure 19. (a) Reflection spectra of single cavity EFPI using a taper, with $OPL_{air} = 0.05, 1, 5, 10, 40$ mm; (b) Fourier spectra for every OPL_{air} measured; (c) corresponding displacement characterization.

From here, I decided to measure a double cavity EFPI by adding a polymer tip to the fiber, as described in Chapter 3. The third device we present is a SMF with a NOA81 polymer cap at the fiber end whose distance performance is shown in the next figures. In Fig. 20(a), the optical spectra showed a double modulation interference pattern due to the double cavity configuration (in fact, there are three interference terms, as it was discussed in Chapter 2; the third term is associated to the sum of the first and the second cavity optical path length). These three interference terms should be seen in the Fourier domain (Fig. 20(b)), but since the polymer cavity is too short ($OPL_{pol} = 118\mu m$), only one peak is observed, the air optical path length. This peak presents a noisy signal due to the shape and size of the tip added to the optical fiber; for this reason, we did not continue exploring this type of device. By tracking the position of this peak, we can plot a displacement characterization curve, as shown in Fig. 20(c). The dynamic range was 67 mm, almost seven times larger than that of a conventional EFPI.

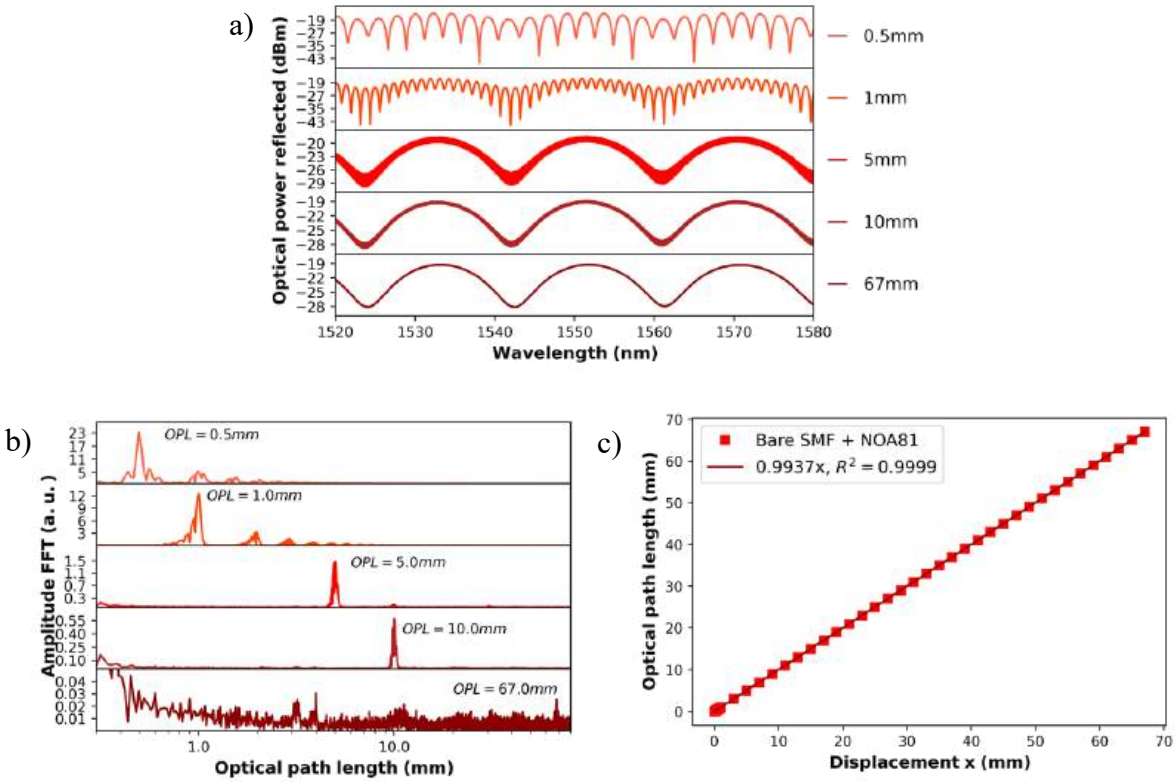

Figure 20. (a) Reflection spectra of double cavity EFPI using a bare SMF with NOA81, with $OPL_{air} = 0.05, 1, 5, 10, 67$ mm. (b) Fourier spectra for every OPL_{air} measured; (c) corresponding displacement characterization.

I present every device used to characterize the displacement performance corresponding to its dynamic range, from lower to higher. The next device is a SMF FC/PC connector with a polymer cap attached to the ferrule connector. This configuration obtained the best performance [14], which is why I used two different polymers (NOA81 and PDMS) with two different cavity lengths in order to compare each other and conclude which parameters are more convenient to use.

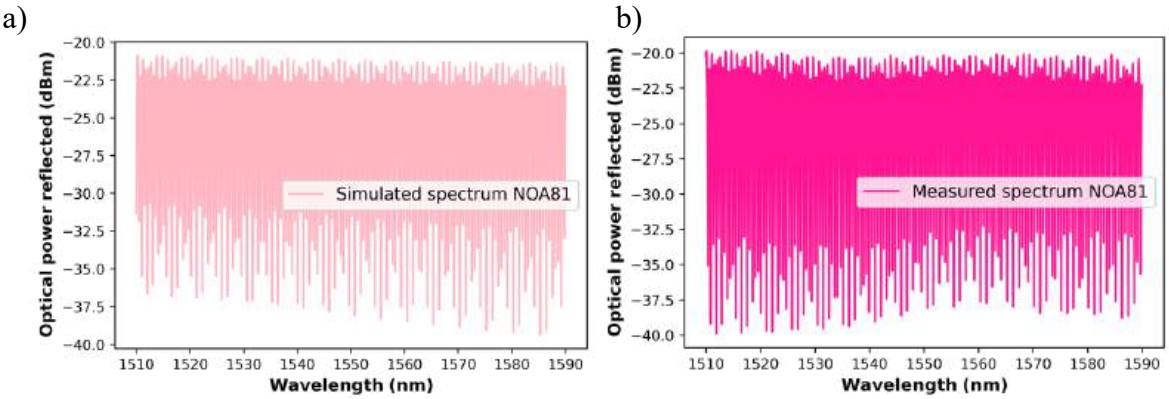

Figure 21. (a) Simulated and (b) experimental reflection spectra of a PC-FFPI using NOA81.

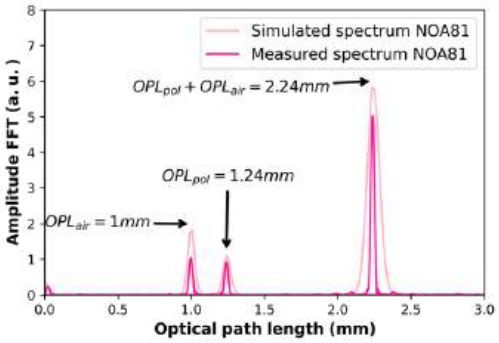

Figure 22. Simulated and experimental Fourier spectra of a PC-FFPI using NOA81.

Considering the theoretical model presented in Section 2, I simulated the reflection intensity of the cascaded PC-FFPI sensor; the parameters used in the simulations are for NOA81: L_{pol}=0.86mm, L_{air}=1mm, n_{pol}=1.54, R=1.023mm, R_1=0.0009, R_2=0.045, R_3=0.95; and for PDMS: L_{pol}=0.53mm, L_{air}=1mm, n_{pol}=1.39, R=1.194mm, R_1=0.0003, R_2=0.025, R_3=0.95; in both cases n_{air}=1.00. The simulated spectrum for NOA81 is shown in Fig. 21(a) and the corresponding Fourier transform is shown in the light pink spectrum shown in Fig. 22. Using the experimental set-up shown in Fig. 17, I proceed to replicate the conditions of the simulations; as can be seen, the optical spectrum (Fig. 21 (b)) and Fourier spectrum (dark pink in Fig. 22) are in good agreement with the simulated spectra.

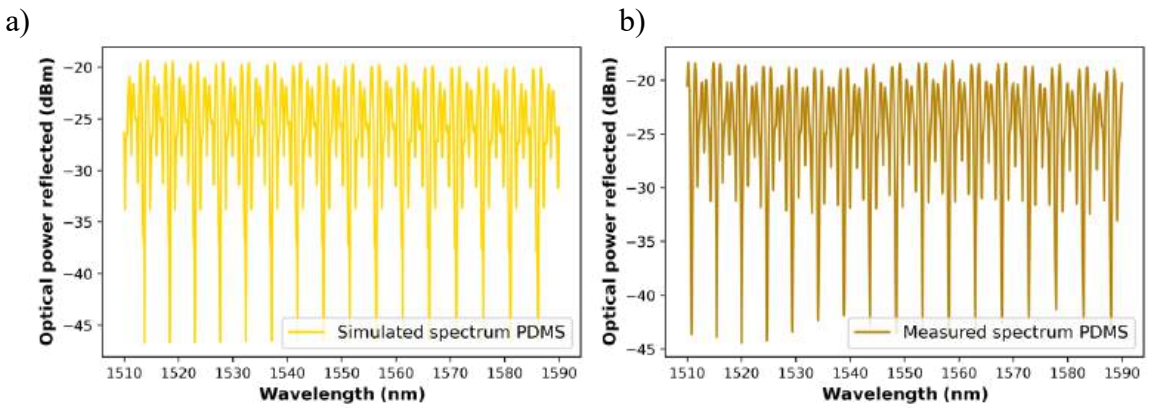

Figure 23. (a) Simulated and (b) experimental reflection spectra of a PC-FFPI using PDMS.

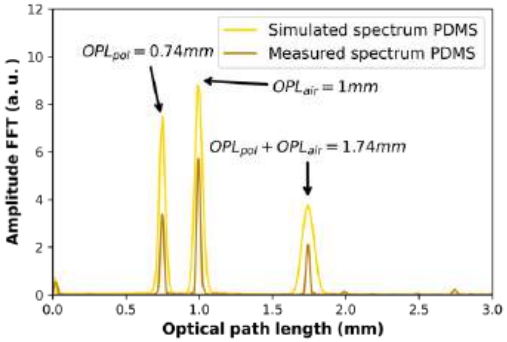

Figure 24. Simulated and experimental Fourier spectra of a PC-FFPI using PDMS.

In the same way, the simulated spectrum for PC-FFPI using PDMS is shown in Fig. 23(a), and the corresponding Fourier transform is shown in the light yellow spectrum shown in Fig. 24. The experimental spectrum shown in Fig. 23(b) and the Fourier spectrum (dark yellow in Fig. 24) are in good agreement with the simulated spectra, so it is possible to assume that the theoretical model proposed here to determine the coupling coefficient is a good approximation to describe the principle of operation of the EFPI proposed in this work. The complete process of the displacement characterization of the modified EFPI is shown in the following section.

First, I present a PC-FFPI with a NOA81 tip of $OPL_{pol} = 1.24mm$. Fig. 25(a) shows the optical domain spectra at different air-cavity lengths. The Fourier spectrum when the air-cavity length was 5 mm is shown in Fig. 25(c). Now, we can observe three peaks corresponding to the air cavity, the polymer cavity, and the air + polymer cavity. Fig. 25(d) shows the Fourier spectrum for an air cavity of 94 mm length, which corresponds to the upper limit of the dynamic range, around 9 times larger than that obtained with a conventional EFPI using a SMF tip. By tracking the position of the third peak of the Fourier spectrum (the higher amplitude peak), we can obtain the displacement characterization curve, as shown in Fig. 25(b).

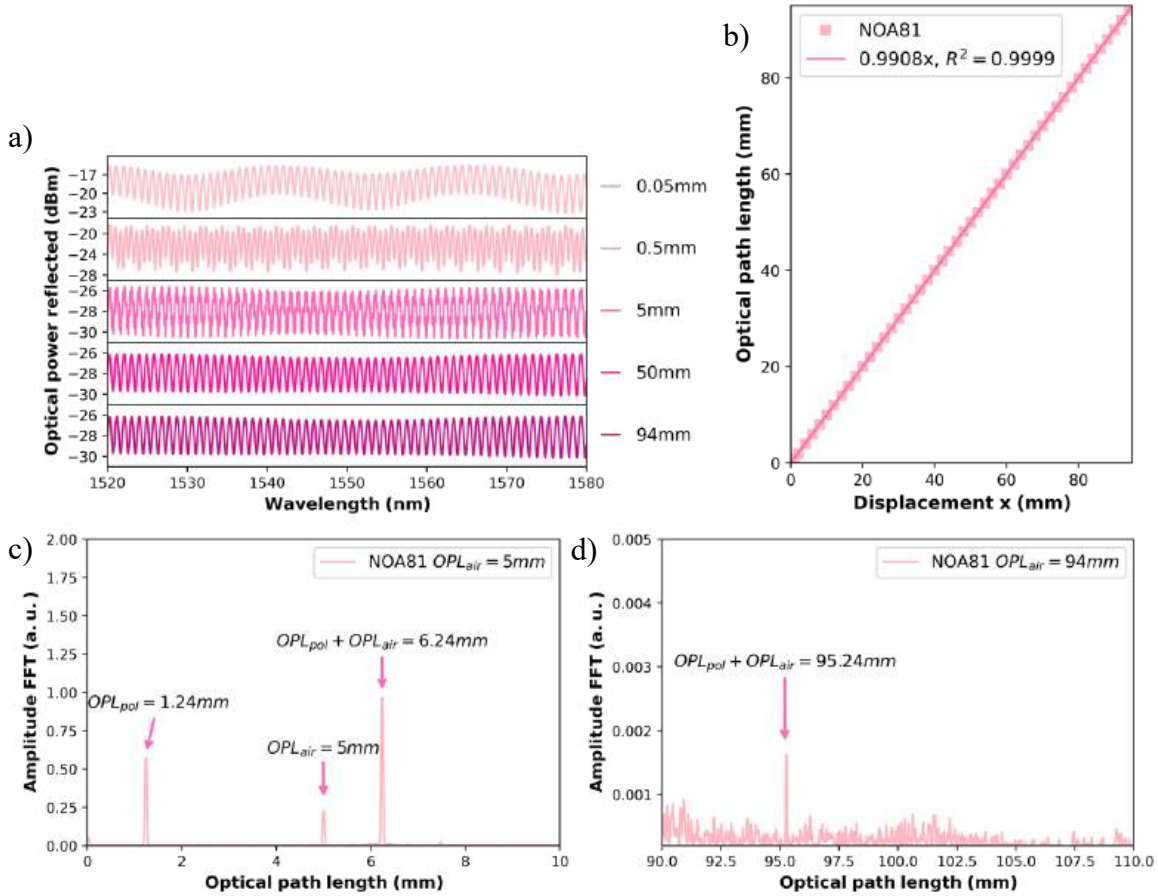

Figure 25. (a) Reflection spectra of a PC-FFPI using NOA81, with $OPL_{pol} = 1.24$mm and $OPL_{air} = 0.05, 0.5, 5, 50, 94$ mm, (b) corresponding displacement characterization. Fourier spectra for (c) $OPL_{air} = 5$ mm and (d) $OPL_{air} = 94$ mm.

Then, I present a PC-FFPI with a PDMS tip of $OPL_{pol} = 0.7473\ mm$. In Fig. 26(a), we show the optical domain spectra at five different air-cavity lengths. In Fig. 26(c), we show the Fourier spectrum when the air-cavity length was 5 mm. In this spectrum, the third peak is the one with the smallest amplitude; the curvature of the polymer surface also increases the intensity of the beam reflected, but this seems to increase the difference in the intensity of the two interfering beams. Fig. 26(d) shows the Fourier spectrum for an air cavity of 87 mm length, corresponding to the dynamic range's upper limit. By tracking the position of the second peak of the Fourier spectrum, we can obtain the displacement characterization curve presented in Fig. 26(b).

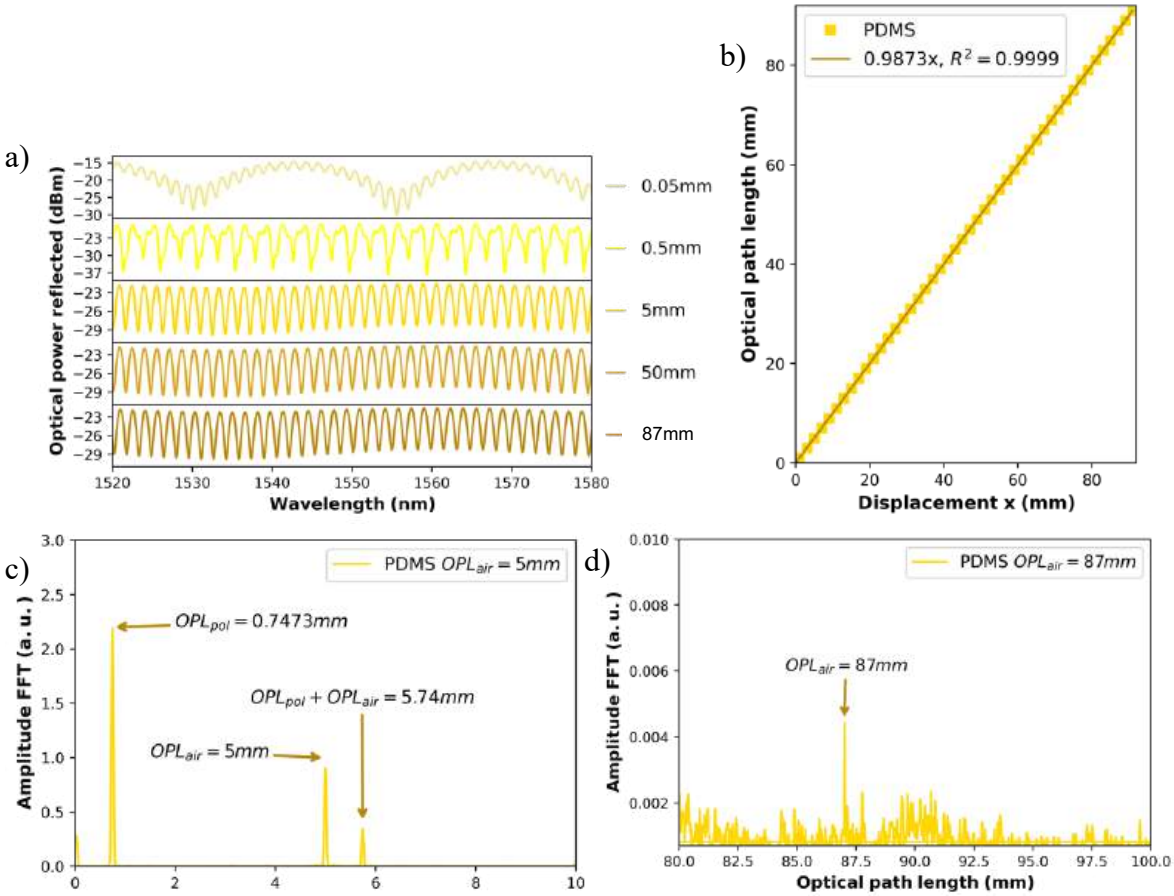

Figure 26. (a) Reflection spectra of a PC-FFPI using PDMS, with $OPL_{pol} = 0.7473$ mm and $OPL_{air} = 0.05, 0.5, 5, 50, 89$ mm, (b) corresponding displacement characterization.. Fourier spectra for (c) $OPL_{air} = 5$ mm and (d) $OPL_{air} = 87$ mm.

I made three independent tests to study the accuracy of the displacement measurement of the PC-FFPI with NOA81 cap, starting at the same initial value; the results are presented in Fig. 27. It is possible to assume that the same displacement measurement was obtained. I made all measurements in the laboratory without temperature control. Temperature affects the refractive index and length of the polymers. In a PC-FFPI, temperature changes produce a displacement of the interference pattern, but not in the OPL of the PDMS cavity since no displacement has been observed in the peak in the Fourier domain in a temperature range from −10 to 45 °C [20]. Therefore, it is possible to state that distance measurements are not affected by temperature changes in that range.

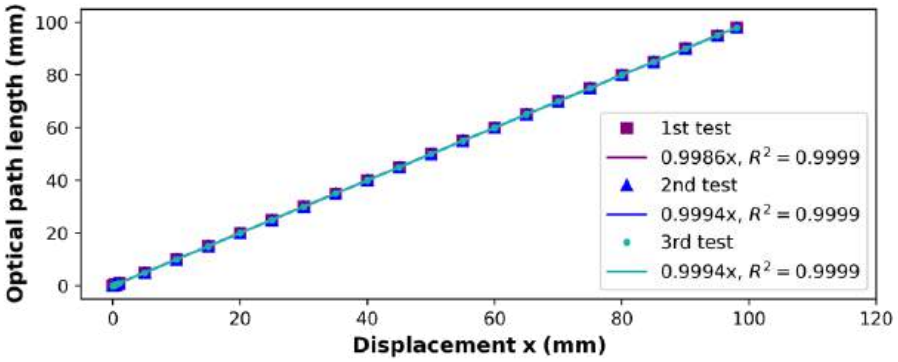

Figure 27. Displacement characterization curve of three tests made with the PC-FFPI with a NOA81 cap.

Using a secondary scale in measuring equipment and instruments, such as calipers, increases the resolution and reduces the uncertainty of measurements. The optical version of the Vernier effect relies on the combination of two interferometers, where the interferometric signals can be seen as the Vernier scales.

Employing the experimental set-up presented in Fig. 17 (double cavity PC-FFPI), we can measure nano-displacements using the Vernier effect, which is the combination of two interference spectra with free spectral range (FSR) slightly different to produce a secondary scale envelope with larger FSR in the resulted spectrum, as shown in Fig. 3. I followed a methodology reported in [32] to generate an envelope associated with the Vernier effect. The main condition of the Vernier effect is to set the OPL of both cavities equal, i.e., $OPL_{pol} = OPL_{air}$. When this condition is fulfilled, I measured the reflected intensity, which is used as a reference signal labeled as $I_{ref} = I_{PC-FFPI}$. I considered the polymer cavity the reference cavity with a constant OPL. Meanwhile, the air cavity is the sensing cavity. Then, I applied a small change in the air cavity length $OPL_{air} = OPL_{pol} + \rho$, where $\rho \ll OPL_{pol}$, and the spectrum obtained is labeled as $I_\rho = I_{PC-FFP}$. To highlight the envelope changes produced in the reflected intensity by the increment ρ in the OPL of the air cavity, it is necessary to compare the spectrum of I_{ref} with I_ρ through the subtraction operation $I_{sensing} = I_\rho - I_{ref}$. I followed this procedure to analyze the response of the PC-FFPI for three different initial values of ρ, and at each position, I applied several nano-displacements (δ) of the mirror surface with respect to the SMF connector. Fig. 28(a), 29(a), and 30(a) show the spectra of $I_{sensing}$ when $\rho_1 = 30\mu m$, $\rho_2 = 40\mu m$, and $\rho_3 = 60\mu m$, respectively, for a NOA81 tip and an $OPL_{pol} = 1.24mm$. The spectra unfold a dense fringe pattern modulated by two envelopes (upper and lower). Here, the upper envelope is highlighted in each spectrum; I tracked the wavelength position of one node of the spectrum every δ displacement to construct the characterization curves shown in Figs. 28(b), 29(b), and 30(b), respectively. The displacement sensitivity was 30.22, 26.04, and 22.23 pm/nm for an initial ρ of 30, 40, and 60 μm, respectively. It is possible to calculate a resolution of 0.66, 0.77, and 0.90 nm, respectively, considering that the resolution of the sm125 interrogator is 20 pm. In this way, the lower the value of ρ, the higher the calculated resolution and its sensitivity since both are related.

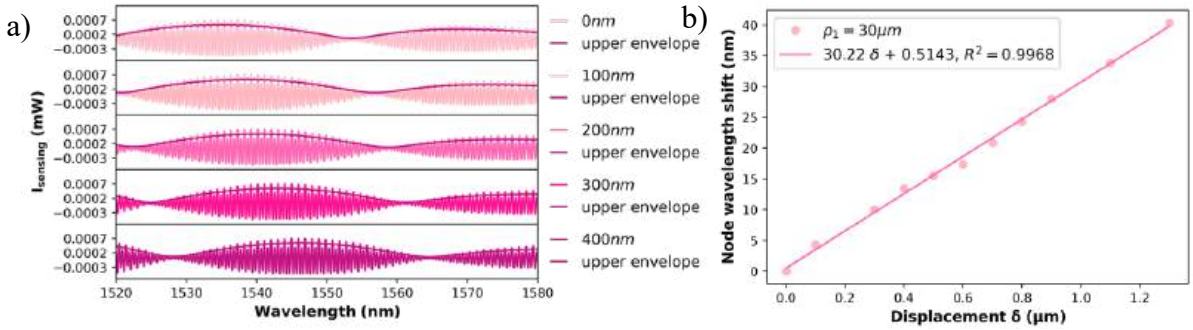

Fig. 28. (a) Spectra of $I_{sensing}$ and (b) the characterization curve of the node wavelength shift for a PC-FFPI with NOA81 cavity of $OPL_{pol} = 1.24mm$ for different displacements δ when $\rho_1 = 30\mu m$.

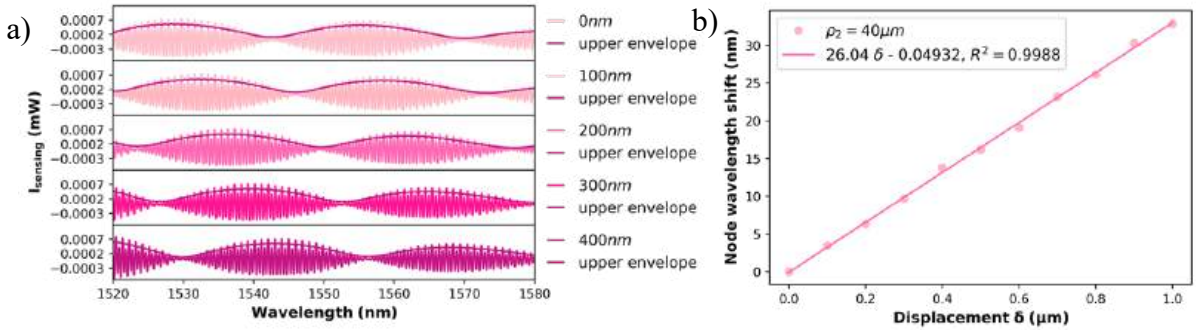

Fig. 29. (a) Spectra of $I_{sensing}$ and (b) the characterization curve of the node wavelength shift for a PC-FFPI with NOA81 cavity of $OPL_{pol} = 1.24mm$ for different displacements δ when $\rho_2 = 40\mu m$.

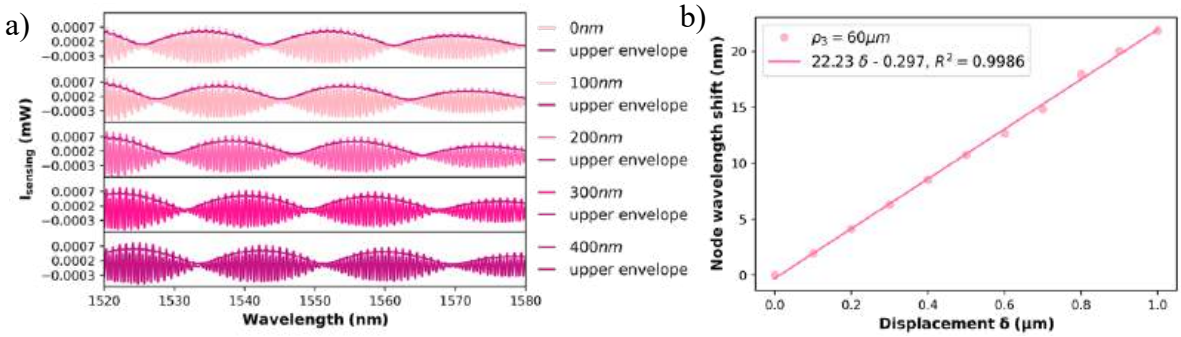

Fig. 30. (a) Spectra of $I_{sensing}$ and (b) the characterization curve of the node wavelength shift for a PC-FFPI with NOA81 cavity of $OPL_{pol} = 1.24mm$ for different displacements δ when $\rho_3 = 60\mu m$.

Figs. 31(a), 32(a), and 33(a) show the measured spectra when $\rho_1 = 20\mu m$, $\rho_2 = 30\mu m$, and $\rho_3 = 40\mu m$ respectively for a PDMS tip with an $OPL_{pol} = 0.7473mm$; and for displacements of δ = 0, 100, 200, 300, and 400 nm. The characterization curves are shown in Figs. 31(b), 32(b), and 33(b). The sensitivities obtained with this connector were 88.47,

49.82, 40.35 pm/nm, and a corresponding resolution estimated of 0.23, 0.40, and 0.5 nm for initial ρ of 20, 30, and 40 µm, respectively.

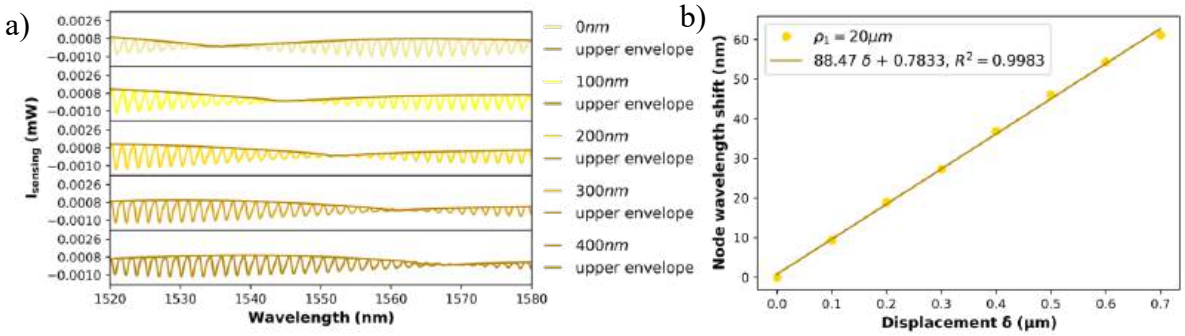

Fig. 31. (a) Spectra of $I_{sensing}$ and (b) the characterization curve of the node wavelength shift for a PC-FFPI with PDMS cavity of $OPL_{pol} = 0.7473\ mm$ for different displacements δ when $\rho_1 = 20\mu m$.

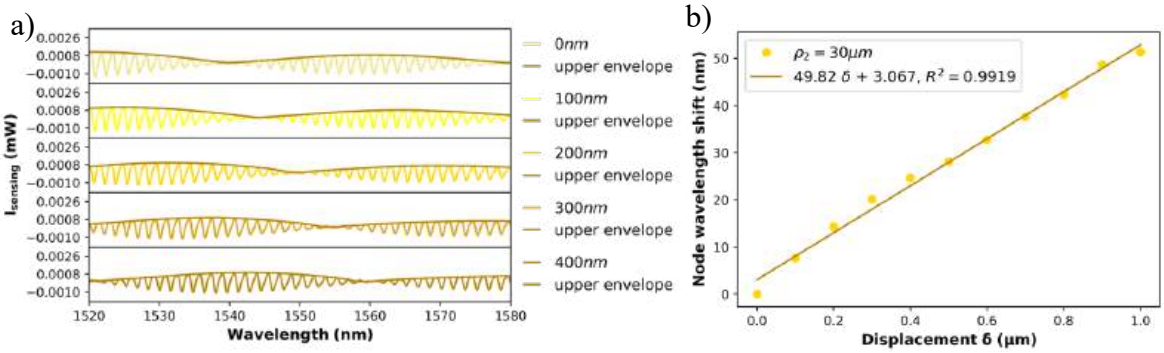

Fig. 32. (a) Spectra of $I_{sensing}$ and (b) the characterization curve of the node wavelength shift for a PC-FFPI with PDMS cavity of $OPL_{pol} = 0.7473\ mm$ for different displacements δ when $\rho_2 = 30\mu m$.

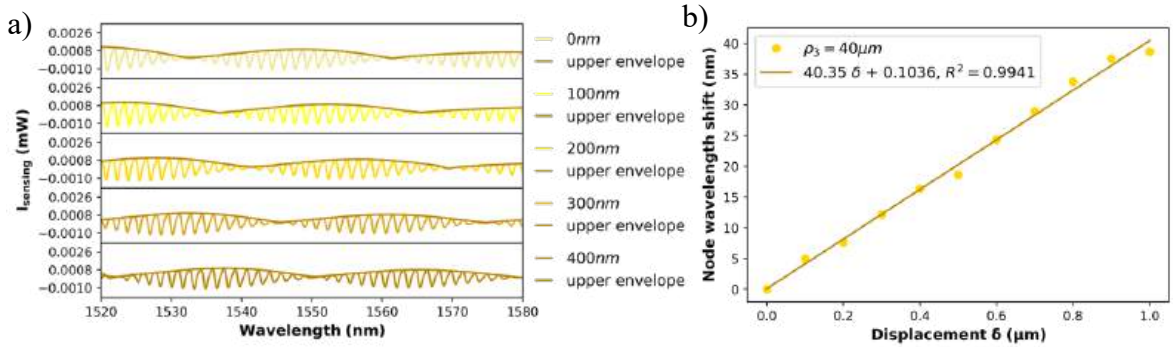

Fig. 33. (a) Spectra of $I_{sensing}$ and (b) the characterization curve of the node wavelength shift for a PC-FFPI with PDMS cavity of $OPL_{pol} = 0.7473\ mm$ for different displacements δ when $\rho_3 = 40\mu m$.

Comparing the response of the two devices, the connector with NOA81 (smaller curvature radius) presents a wider dynamic range (94mm), while that with the PDMS (bigger curvature

radius) tip has a higher resolution (0.23nm). Moreover, in both cases the dynamic range and the resolution are improved compared with a conventional EFPI using a SMF tip.

It is possible to increase the sensitivity and resolution of this displacement sensor using a light source with a broader span because we can track the nodes in a wider space. In this sense, the interferometer proposed here is reconfigurable and can be adapted to the requirements of the measurement conditions. Nano-displacement measurements must consider the temperature cross-sensitivity since temperature changes produce the envelope shift. For this application, the ambient temperature must be controlled during the measurement, or the polymer must be replaced with another material with lower temperature sensitivity.

CHAPTER 5: TEMPERATURE MEASUREMENT

Fiber optic-based temperature sensors (FOTS) have gained attention since it has been demonstrated that they can reach the competitive levels of sensitivity, response time, dynamic range, or resolution demanded. They are also attractive due to their size and lightweight, the immunity against electromagnetic external noise, the low chemical reactivity, and the biocompatibility of the glass used to fabricate the fiber optics [33], [34]. FOTS, like most sensing technologies, must deal with the compromise between sensitivity and dynamic range. Some strategies have been applied to improve the temperature sensitivity of FOTS as: the fabrication of fiber optic devices where highly sensitive optical phenomena, such as interference or plasmonic resonance, can be generated steadily using specialty fibers (hollow core fiber, photonic crystal fiber, or polarization maintaining fiber) [35], [36], [37]; the inclusion of materials with a high thermo-optic coefficient [38], [39], [40]; the implementation of fiber optic structures or schemes to generate the optical Vernier effect [41], [42], [43]; or more recently, a very successful method is using fiber optic interferometers coated with a polymer to enhance the optical phase difference of the beams involved [38], [39], [40], [44], [45], [46], [47].

The PC-FFPI is one of the simplest FOTS proposed so far; it is very easy to fabricate, especially when transparent photocuring or thermal curing polymers, such as the NOA or PDMS, are used. The polymer attached to the fiber optic tip acts as a Fabry-Pérot cavity; the thickness and refractive index of the polymer cavity are affected by temperature changes. Increments or decrements in temperature modify the phase difference of the interference beams. The polymer response to temperature changes determines the temperature sensitivity of the PC-FFPI; therefore, the only way to enhance the sensitivity of the PC-FFPI is by choosing one with a high thermo-optic coefficient (TOC) or a high thermal expansion coefficient (TEC).

Highly sensitive temperature sensors, despite their small dynamic range, are very appreciated in biomedical applications [48], structural health monitoring [49], and marine environment monitoring [50], to mention a few. It is evident that for some of these applications, the head of the FOTS must be packaged to make them more robust to resist hostile environments or the manipulation of untrained final users in order to extend the use lifetime. Packaging considerably increases the size of a fiber optic thermometer.

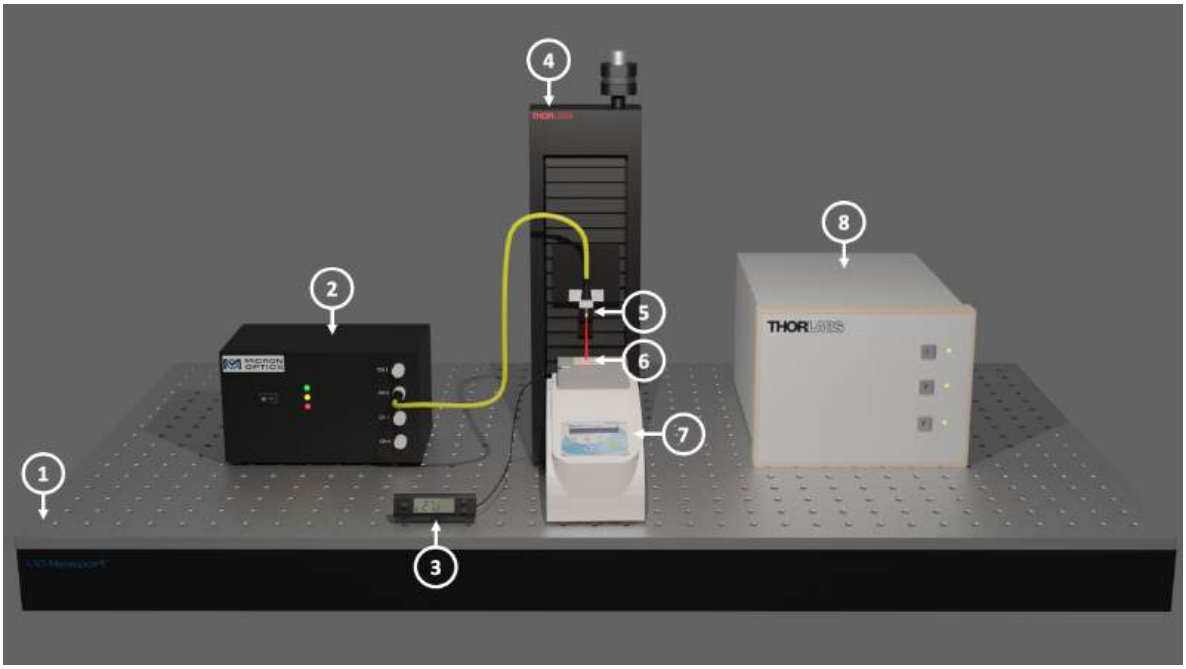

Figure 34. Experimental set-up for temperature characterization: 1. Optical table. 2. The sm125 interrogator. 3. Digital thermometer with thermocouple. 4. Motorized translation stage (1-axis). 5. Ferrule connector with polymer tip. 6. Mirror 7. Dry bath with block. 8. Stepper motor controller.

In this chapter, I report the implementation of a PC-FFPI and the response of the device subjected to several characterizations in order to obtain a reproducible method to measure temperature changes. Using a set-up presented in Fig. 34, I exposed each of the PC-FFPI made with two different polymers, PDMS and NOA81, to temperature variations. Since the thermal transfer from the heated block to the polymer tip is contactless, I put a thermometer close to the PC-FFPI to obtain an accurate PDMS and NOA81 cap temperature reading. First, since NOA81 has an extensive temperature range (-15 ºC to 80 ºC after being cured), I measured this tip by increasing and decreasing temperature variations between 20 ºC and 70 ºC. When the temperature rises, the optical spectra of the PC-FFPI intensity reflection shift to larger wavelengths, as seen in Fig. 35(a). I tracked the wavelength position of one maximum of the interference pattern near 1550 nm and these values were used to construct the light pink plot in Fig. 35(b). I followed the same maximum when the temperature went down and plotted the dark pink points in Fig. 35(b). The experimental points are fitted by linear regression, with slopes of 0.29 nm/ºC for the rising temperature and 0.42 nm/ºC for the falling temperature. Both slopes should be very similar, but they are not for this case because of the high response to humidity of the optical adhesive NOA81. To avoid hysteresis in this analysis, we heated the tip to 60 ºC for 30 minutes before increasing and decreasing the temperature. After that dry process, we made the corresponding measurements again and obtained two closed slopes, as desired, with values of 0.45 nm/ºC (increasing T) and 0.47 nm/ºC (decreasing T), as shown in Fig. 35(c).

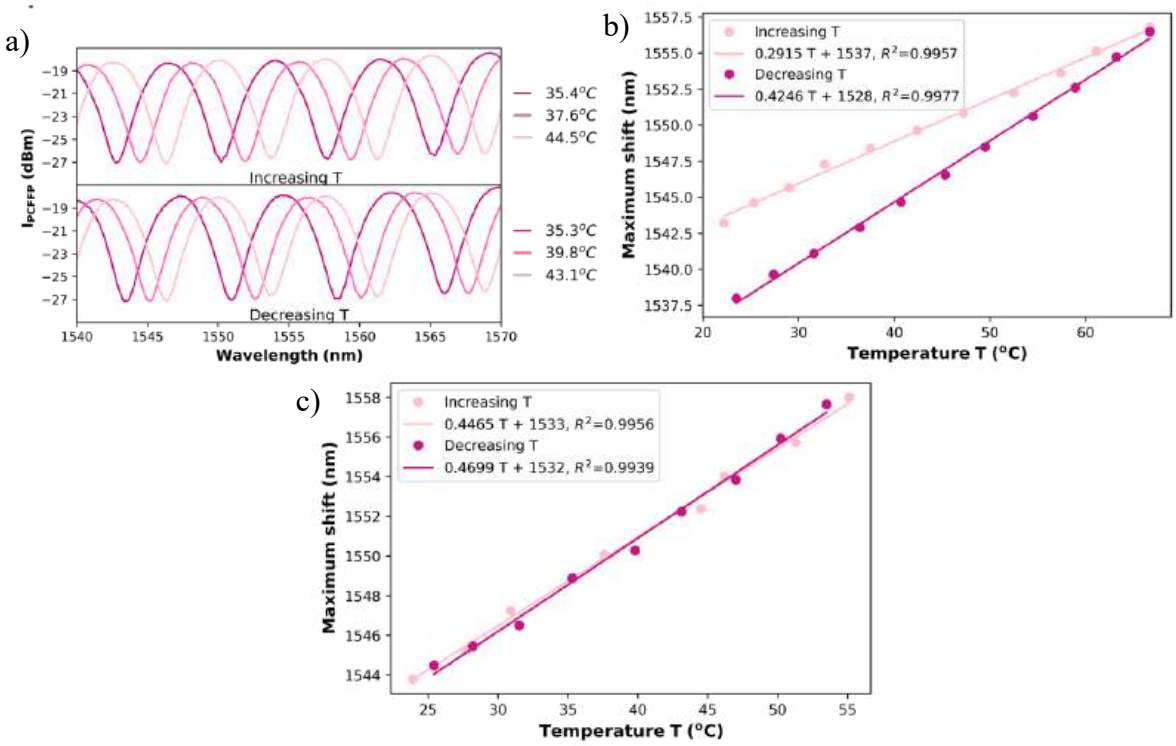

Figure 35. (a) Spectra of the measured I_{PCFPI} and the characteristic curve of the wavelength shift for a PCFPI with a NOA81 cavity (b) before and (c) after the dry process.

In the same way, I tested a second PCFPI tip using PDMS, which has a shorter temperature range (-10ºC to 60 ºC after being cured). I measured this tip by increasing and decreasing temperature variations between 30 ºC and 36 ºC. The optical spectra of the PCFPI intensity reflection shift to larger wavelengths as the temperature increases, as seen in Fig. 36(a). Tracking one maximum of the interference pattern, I obtained the characteristic curve of the plotted points at different increasing and decreasing temperature values, as shown in Fig. 36(b). The slope when the temperature rises is 0.54 nm/ºC (light yellow), and the slope when the temperature falls is 0.58 nm/ºC (dark yellow). The device temperature sensitivity is very similar when the temperature increases or decreases. I didn't need to dry the tip to avoid hysteresis. That is the reason we chose the PDMS as the polymer tip for the PCFPI for the following analysis.

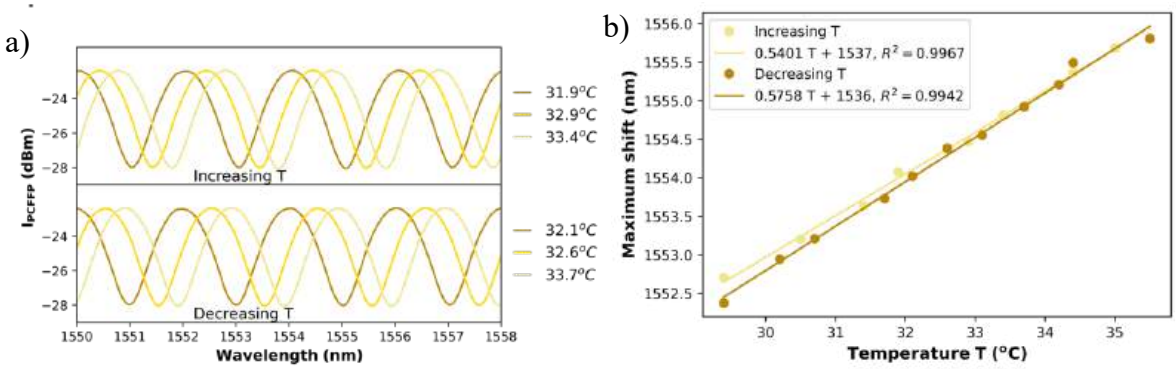

Figure 36. (a) Spectra of the measured I_{PCFPI} and (b) the characteristic curve of the wavelength shift for a PCFPI with a PDMS cavity.

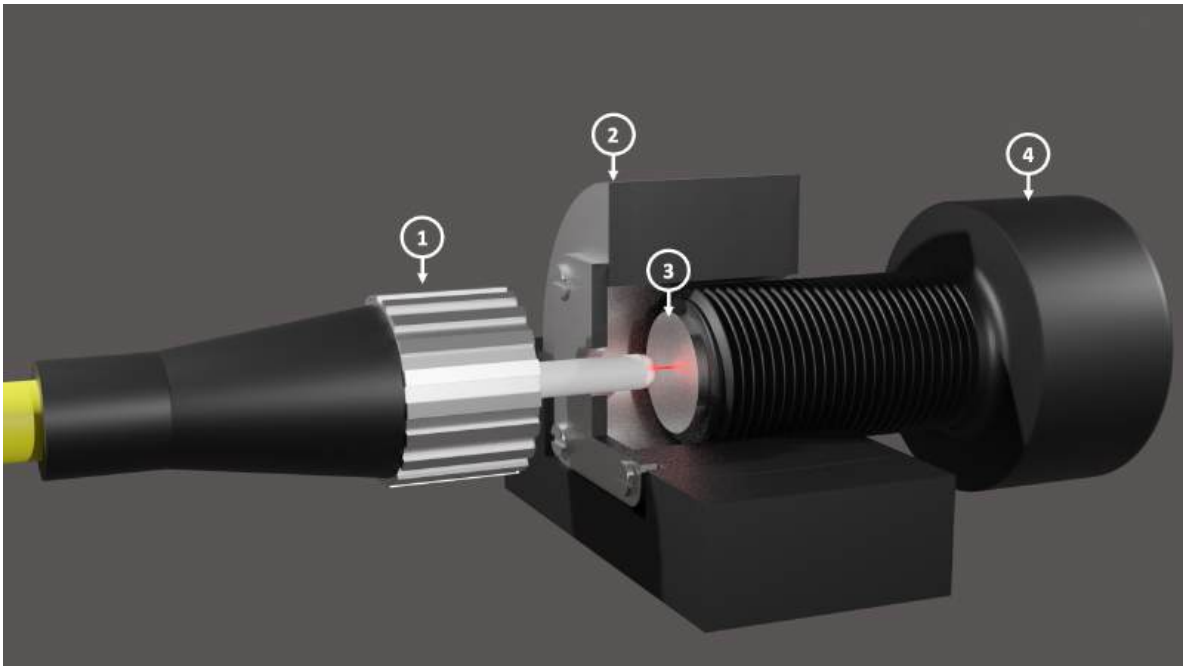

Figure 37. Components of the DCFPI sensor head: 1. Ferrule connector with a polymer cap. 2. Aluminum mount. 3. Plane mirror with a circular shape. 4. Fine thread screw.

It has been demonstrated that the PC-FFPI has a good temperature sensitivity (0.58 nm/ºC). I propose constructing a highly sensitive fiber optic temperature sensor based on a double-cavity Fabry-Pérot interferometer (DCFPI) to generate the Vernier effect and enhance PCFPI sensitivity. The DCFPI is formed when the PCFPI is placed in front of a reflective surface, as shown in Fig. 37. To generate the Vernier effect, it is necessary to set the *OPL* of both cavities nearly equal, i.e., $OPL_{pol} \approx OPL_{air}$. The slight difference in the length of the cavities can be expressed as $OPL_{air} = OPL_{pol} + \rho$, where $\rho \ll OPL_{pol}$.

The optical path lengths of the polymer and air cavity are described by $OPL_{pol} = n_{pol}L_{pol}$ and $OPL_{air} = n_{air}L_{air}$, respectively, and $OPL_{pol} + OPL_{air} = n_{pol}L_{pol} + n_{air}L_{air}$ are the *OPL* of the dual cavity. However, the refractive index of the polymer n_{pol} and the length of the polymer cap L_{pol} are modified by the temperature (*T*) effect as follows [51]:

$$n_{pol}(T) = n_0(T_0) + \left(\frac{\partial n_{pol}}{\partial T}\right)_{T=T_0}(T - T_0), \tag{67}$$

$$L_{pol}(T) = L_0(T_0)[1 + \alpha_T(T - T_0)], \tag{68}$$

Where T_0 is the initial temperature, $\partial n_{pol}/\partial T$ is the thermo-optic coefficient (*TOC*) and α_T the thermal expansion coefficient (*TEC*). For PDMS, $TOC = -4.5 \times 10^{-4}\ ^{o}C^{-1}$ and $TEC = 9.6 \times 10^{-4}\ ^{o}C^{-1}$ [52].

Using (67), (68), and the theoretical model presented in Section 2, we simulated the reflection intensity of the cascaded PC-FFPI sensor; the parameters used in the simulations are for PDMS: L_{pol}=0.58mm, L_{air}=0.84mm, n_{pol}=1.39, R=1.127mm, R_1=0.0006, R_2=0.025, R_3=0.95, and n_{air}=1.00. The coupling coefficients at a wavelength $\lambda = 1550\ nm$ are $\eta_1 = 0.1027$ and $\eta_2 = 0.0544$. The slight difference in the OPL of air and polymer cavities ρ was set equal to 30 µm since this value assures the observation of two nodes in the wavelength span from 1510 to 1590 nm, the emission band of the interrogator used in this work. The simulated spectrum of the DCFPI, assuming a temperature of 26.7 ºC, is shown in Fig. 38(a), and its corresponding experimental spectrum is shown in Fig. 38(c). When we consider an increment of 0.1 °C in the ambient temperature, the *OPL* of the polymer cavity is changed, and the simulated and experimental spectra (shown in Fig. 38(b) and Figure 38(d), respectively) are red-shifted concerning the spectra of Fig. 38(a) and Fig. 38(c).

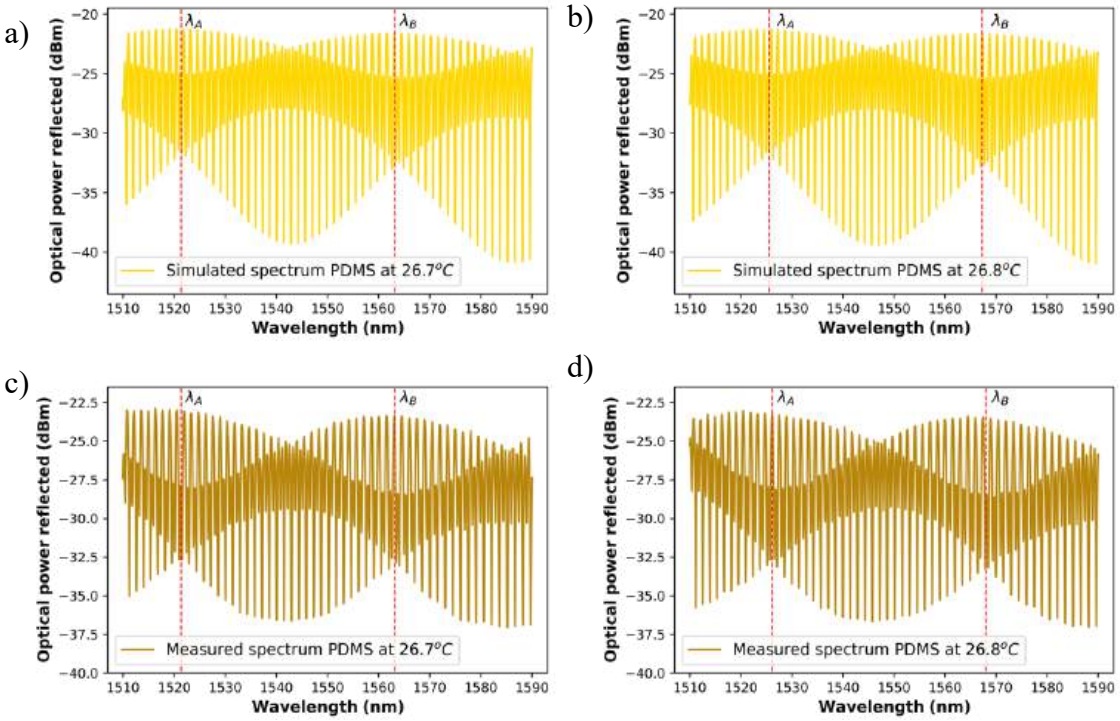

Figure 38. (a,b) Simulated and (c,d) experimental reflection spectra of a DCFPI using PDMS for temperature values of 26.7 ºC and 26.8 ºC, respectively.

The procedure to construct the DCFPI is illustrated in detail in Figure 37. First, we inserted the ferrule with the polymer cap (1) through the hole machined and fixed it to threaded fiber adapted in the aluminum case (2). I approached a circular mirror (3) glued to the tip of a screw (4) to the polymer cap by driving the screw through the nut machined on the other side of the case. These elements constitute the head of the DCFPI. I adjusted the length of the air cavity between the polymer cap and the mirror by moving the screw.

In the same way as the PCFPI fabrication process, we used the sm125 interrogator and its automated program to calculate the *OPL* of the air cavity to adjust the small difference ρ between the *OPL* of the air and polymer cavities and generate the Vernier effect. Since the thread of the screw is fine, it is possible to set the mirror in front of the polymer cap accurately. The ρ value is directly related to the temperature sensitivity of the DCFPI sensor. In our case, we set ρ around 30 μm measured through the FFT; this is the most appropriate value to obtain the maximum sensitivity without losing the chance to track two nodes in each spectrum in the wavelength span from 1510 to 1590 nm. Using a light source with a broader span, it is possible to increase the sensitivity and dynamic range of this temperature sensor by reducing the value of ρ.

We placed the DCFPI sensor head above a metal block in the Benchmark dry bath to set the temperature changes and perform its characterization. We used a digital thermometer near our DCFPI to monitor the temperature of the surroundings. The SMF was connected to an ENLIGHT MicronOptics interrogator sm125 to collect the reflection spectra.

I first set the temperature of the dry bath to 35 ºC, then I turned off the equipment. As the temperature decreased, I recorded the spectrum of the DCFPI, and the temperature assigned to each spectrum according to the digital thermometer placed on the side of the DCFPI. The optical spectrum shows a dense fringe pattern where two nodes can be identified (see Figures 39(a), 40(a), 41(a), and 42(a)). The nodes shift toward shorter wavelengths as the temperature decreases. Tracking the wavelength position of the nodes through the frame, it is possible to plot the temperature characterization curve of nodes, as shown in Figures 39(b), 40(b), 41(b), and 42(b). It is complicated to track the displacement of a single node in a wide range of temperatures due to the high sensitivity of the Vernier effect. However, since two nodes are present in the optical spectra, we can track both by considering the overlap between the two characteristic curves. It was possible to follow four different nodes by their overlap (Figures 39–42). Tracking the nodes' displacement in the spectra could allow us to estimate the temperature variations but not to identify which node is related to a particular temperature range. For instance, the position of the nodes at 30.3 ºC (Figure 39(a)) is very similar to that obtained at 29.2 ºC (Figure 40(a)), 28.1 ºC (Figure 41(a)), and 27.1 ºC (Figure 42(a)), but the FSR is 40.3 nm, 41.5 nm, 42.4 nm, 43.4 nm, respectively. The FSR could help us distinguish whether we are following Node 1 or Node 3. The nodes' position and the FSR can be used to avoid the apparent ambiguity in identifying the node and, consequently, the temperature. Thus, a high resolution FOTS with a temperature dynamic range of 26.8 ºC to 31.7 ºC, as seen in Figure 43, was demonstrated.

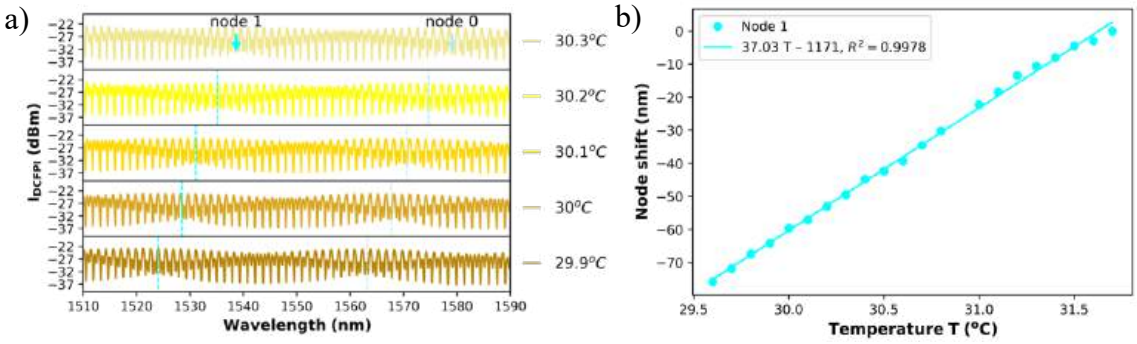

Figure 39. (a) DCFPI measured optical spectra and (b) the characteristic curve of the node wavelength shift in the temperature range of 29.6 ºC to 31.7 ºC.

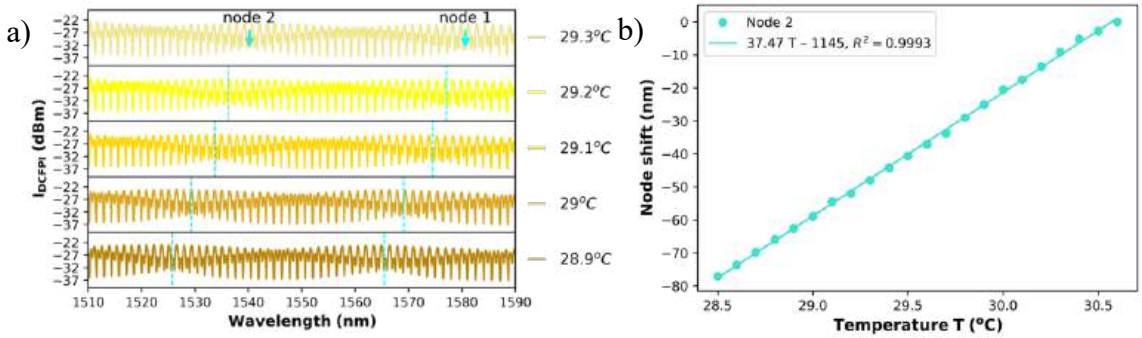

Figure 40. (a) DCFPI measured optical spectra and (b) the characteristic curve of the node wavelength shift in the temperature range of 28.5 ºC to 30.6 ºC.

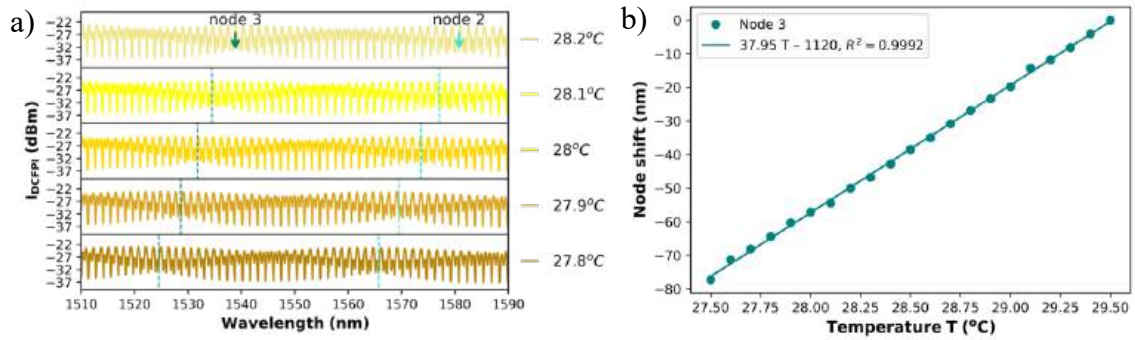

Figure 41. (a) DCFPI measured optical spectra and (b) the characteristic curve of the node wavelength shift in the temperature range of 27.5 ºC to 29.5 ºC.

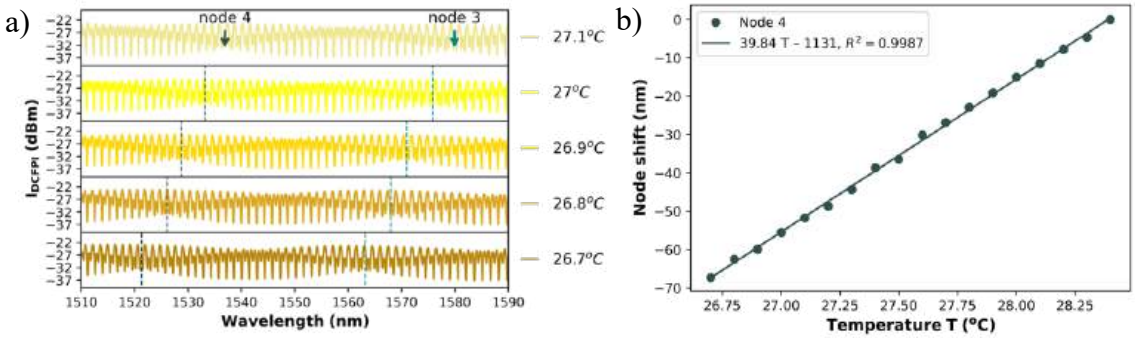

Figure 42. (a) DCFPI measured optical spectra and (b) the characteristic curve of the node wavelength shift in the temperature range of 26.7 ºC to 28.4 ºC.

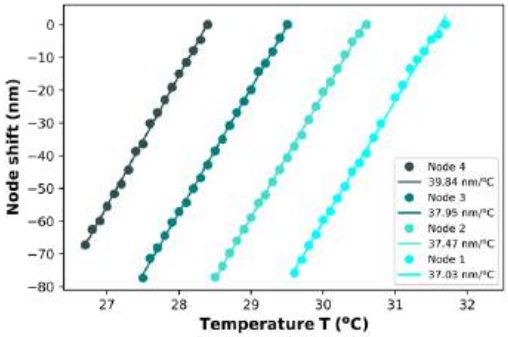

Figure 43. Characteristic curves of the wavelength shifts of 4 nodes for the DCFPI in the temperature range of 26.7 ºC to 31.7 ºC with its respective sensitivity values.

As the temperature decreases, the sensitivity of the device increases since the length of the PCFPI is closer to the air cavity length, and the FSR increases. This is more evident in the temperature range of 26.7 ºC to 28.4 ºC (Figure 42) when sensitivity increases to 39.8 nm/ºC, 69.2 times the sensitivity of a conventional PC-FFPI temperature sensor.

Compared with other FOTS based on the Vernier effect (see Table 2), this device exhibited a competitive sensitivity. Furthermore, the DCFPI possesses other fascinating characteristics that could be attractive for some applications, for example, the simple fabrication process, the robustness provided by the connector, and the possibility to adjust the length of the air cavity by the movement of the mirror to select the sensitivity and dynamic range of the FOTS.

Type	**Sensitivity (nm/ºC)**	**Dynamic Range (ºC)**	**Reference**
Fiber-optic sensor based on cascaded FPIs	0.18	38–100	[53]
PDMS-filled air microbubble FPI	2.70	51.2–70.5	[54]
Parallel FPIs based on dual Vernier effect	7.61	34–39	[55]
Cascaded FPI and a fixed reflective Lyot filter based on the Vernier effect	−14.63	30–32	[56]
Hybrid interferometers with harmonic Vernier effect	−19.22	41–44	[41]
Cascaded polymer-infiltrated fiber Mach-Zehnder interferometers	−24.86	22–29	[57]
Polymer-capped FFPI by Vernier effect (our work)	39.84	26.7–31.7	[58]

Table 2. Temperature sensing performance of recently reported temperature optical fiber sensors.

CHAPTER 6:
MECHATRONIC PLATFORM

Once we proved that the theoretical model presented in Chapter 2 is in good agreement with the experimental results, we searched for a systemized and efficient way to perform all the necessary procedures to minimize errors and improve the experimental process. A critical part of this work is the fabrication process of our tips. However, the good results motivated us to construct an automatic mechatronic platform to fabricate these devices more accurately and with control. Fig. 44 presents an image of the 3D design of the actual platform.

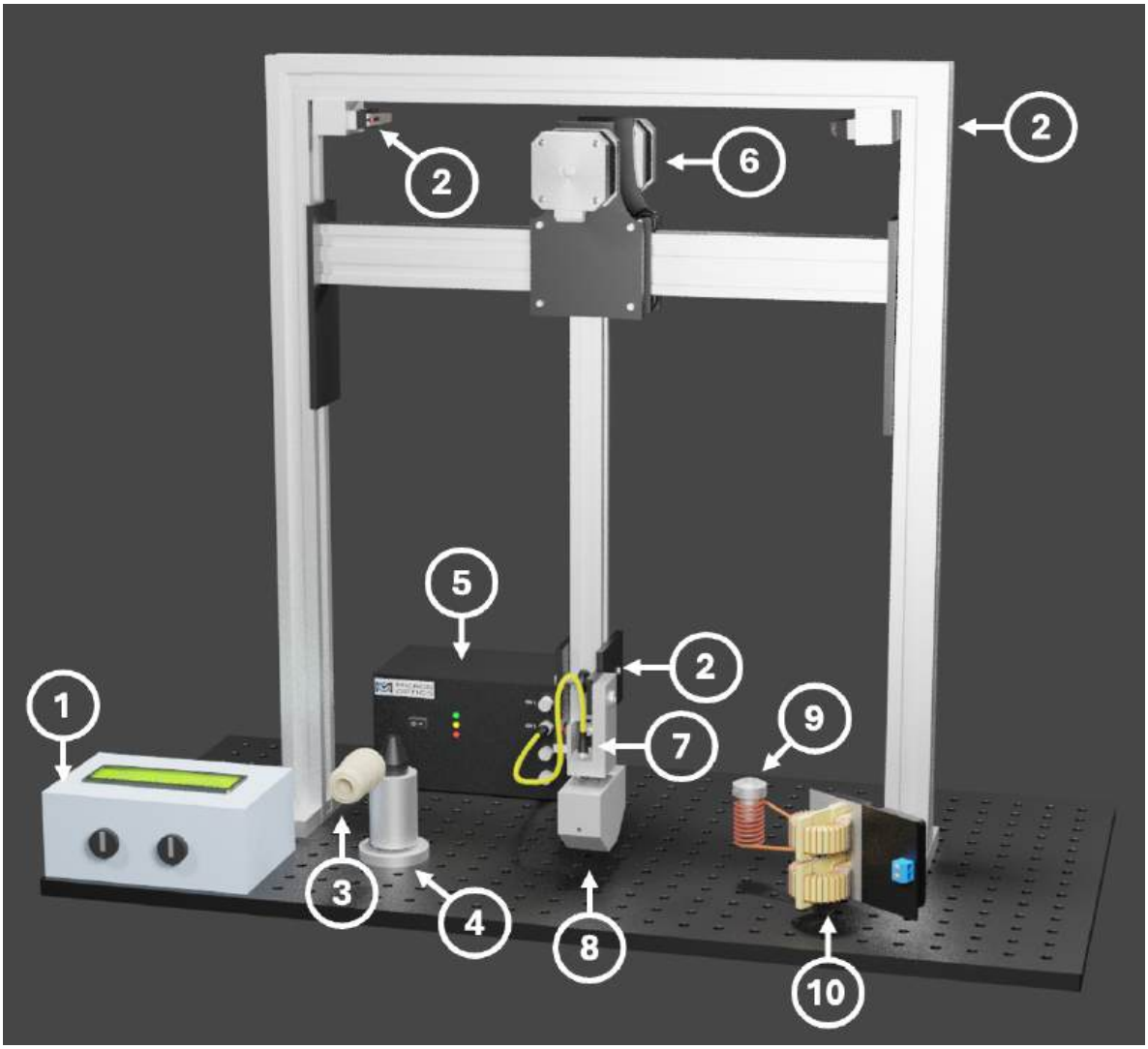

Figure 44. Components of the fabrication mechatronic platform: 1. Interactive control menu operated by Arduino. 2. Limit switches. 3. Digital microscope. 4. Polymer deposit stage. 5. The sm125 interrogator. 6. Bipolar stepper motors. 7. Ferrule connector with polymer tip. 8. UV curing stage. 9. Temperature curing stage. 10. Induction heating module.

As we saw in the last chapter, implementing a self-designed device helps tremendously in a specific task. We build the fabrication tips platform to be able to transfer polymer at the end

of the tip as well as cure the polymer, whether photocurable (as NOA81) or thermocurable (as PDMS); all of this in an automatic way. In Fig. 45 and Table 3, we present every electronic component of the platform labeled with a corresponding letter.

The main element used in this platform is the open-source microcontroller Arduino, which operates all the other elements in a synchronized way. The brain of Arduino is the integrated circuit ATmega328, a microcontroller you can program, erase, and reprogram multiple instructions by the free-access Arduino software. It is very simple to program because it is a simplified version of C++. Besides, it offers a wide range of sensors for many applications. Depending on the number of devices to connect to Arduino, you can choose different boards; in this case, we used the Arduino MEGA version (M) because it offers the highest number of available pins to connect various sensors and actuators. An actuator is a device that transforms hydraulic, pneumatic, or electric energy into physical movement, just as the pair of bipolar stepper motors Nema 17 (D) used in this scheme, one for the horizontal movement of the platform and the other for the vertical motion, both with an angle of step of 1.8^o per step (200 steps per revolution). Each motor needs a driver to control aspects such as the rotation direction and to make the motor programming easier. We decided to use the A4988 driver (K) because it allows us to split up to 16 times the steps of the motors. This means that we can obtain more resolution in the longitudinal movement. We also need two $100\ \mu F$ capacitors, one per motor, to avoid sudden electricity shocks. Once the platform was moving, we needed to set limits for each sense, so we strategically placed three limit switches (O) that also allowed us to set every motion to an initial position, which was very useful when we wanted to set both motors to whatever coordinates. For instance, it is mandatory to place the tip of the bare connector in front of the polymer deposit stage and make contact slowly to transfer the polymer accurately.

After the polymer deposit process comes the curing phase. For the photocuring, we implemented three 3 W UV LEDs (N) with a transistor TIP122 (H) to control its intensity. For the thermal-curing, we conditioned an induction heating coil module (G), also with a TIP122 to control now the temperature. We can measure the temperature of the heating process with a digital thermometer (Q). We displayed the temperature value in a 16x2 LCD that works with an I2C module that reduces the number of connections of the LCD. The display is also used as an interface between the platform and an operator by three rotary encoders (P) to select options as a menu.

Finally, all the components are energized by a 12V/10A AC power source (A) turned on and off with a switch (B). The Arduino MEGA is also fed with the power source by an outlet plug (C). Resistors with different values (J) were used for some components, too.

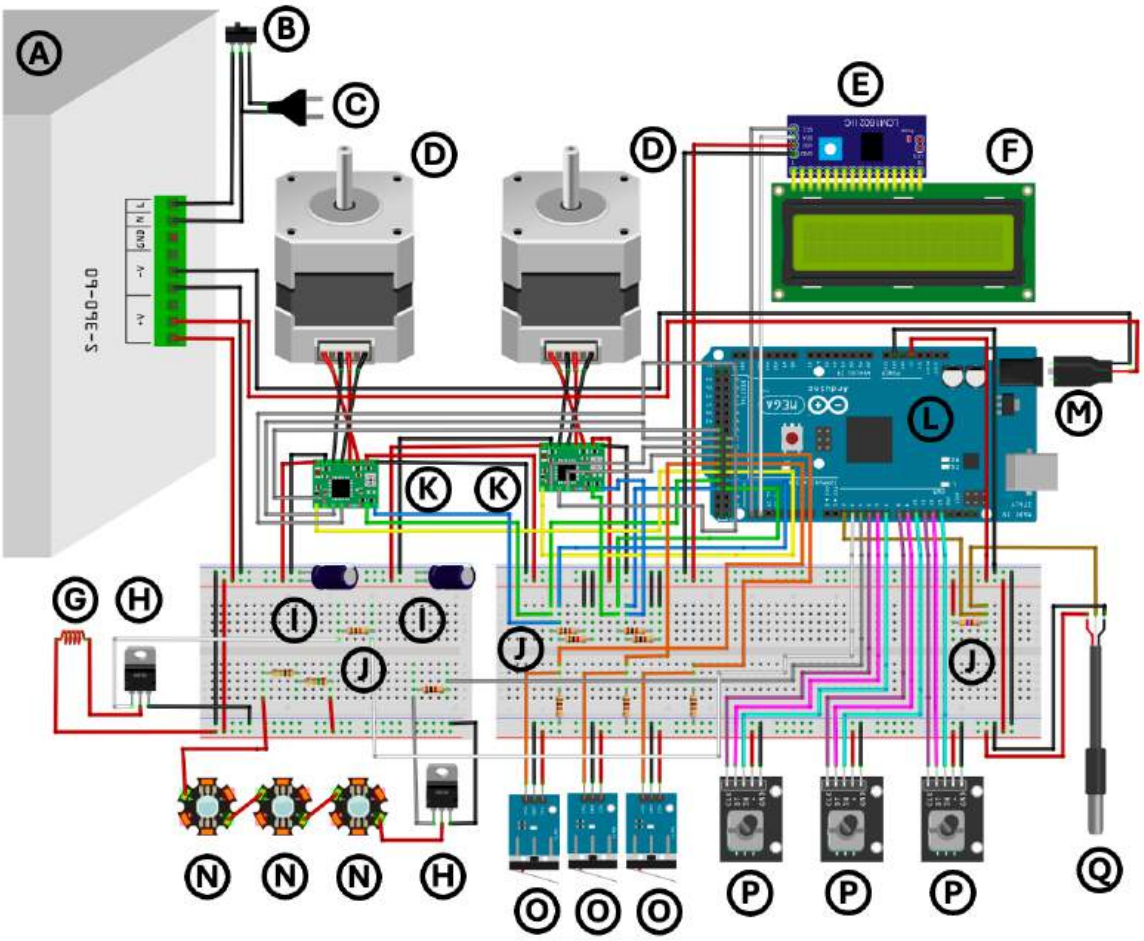

Figure 45. Electronic components of the fabrication mechatronic platform.

Label	**Component**	**Description**
A	Power source	12V/10A/120WAC power source.
B	Switch	Switch to turn the source on or off.
C	Outlet plug	Plug to power up the Arduino.
D	Stepper motors Nema 17	Two stepper motors for the vertical and horizontal displacement.
E	I2C module	Display module to reduce the number of cables.
F	16x2 LCD	Display to control the mechatronic platform menu.
G	Induction heating coil	Induction heating coil for the PDMS curing process.
H	Transistors TIP122	Two transistors TIP122 to regulate the LEDs intensity and coil temperature.
I	Capacitors	Two $100\mu F$ capacitors for each stepper motor.
J	Resistors	One $4.7k\Omega$ resistor, two ceramic resistors (1Ω and 1.5Ω) and nine $1k\Omega$ resistors.
K	A4988 driver	Two stepper motor drivers to control polarity and microstepping.
L	Arduino MEGA 2560	Arduino microcontroller for the general mechatronic platform operation.

M	12V DC plug	DC plug to energize the Arduino.
N	UV LEDs	Three 3W UV LEDs for the NOA curing process.
O	Limit switch	Three limit switches to set the stepper motors to home position.
P	Rotary encoder	Three rotary encoders to manually control the platform menu.
Q	Temperature sensor	DS18B20 digital thermometer to measure and control the coil temperature.

Table. 3. Electronic components of the fabrication mechatronic platform with their corresponding operation function.

The first step of the polymer capped tips fabrication process is to place the fiber connector in its spot, as seen in label 7 of Fig. 44. The general performance of the mechatronic platform is divided into three principal stages: polymer transfer, UV curing, and temperature curing. The polymer transfer stage involves manually placing a polymer drop in a 3D-designed PLA (polylactic acid) container (Fig. 46(a)). We are ready to start the fabrication process once we put the polymer on top of the container. The next step is the UV or temperature curing process, depending on whether we are using NOA81 or PDMS, respectively. If we want to cure a polymer sensible to UV radiation like the NOA81, the automatized operation of the platform carries the fiber connector to the UV curing stage, where three 3W UV LEDs connected in series are inside of an aluminum box, which also works as a heatsink (Fig. 46(b)). Otherwise, if we want to solidify a polymer sensible to heat radiation like the PDMS, we program the platform to carry the fiber connector to the temperature curing stage formed of an aluminum nozzle inside a coil, which will carry out the induction heating (Fig. 46(c)).

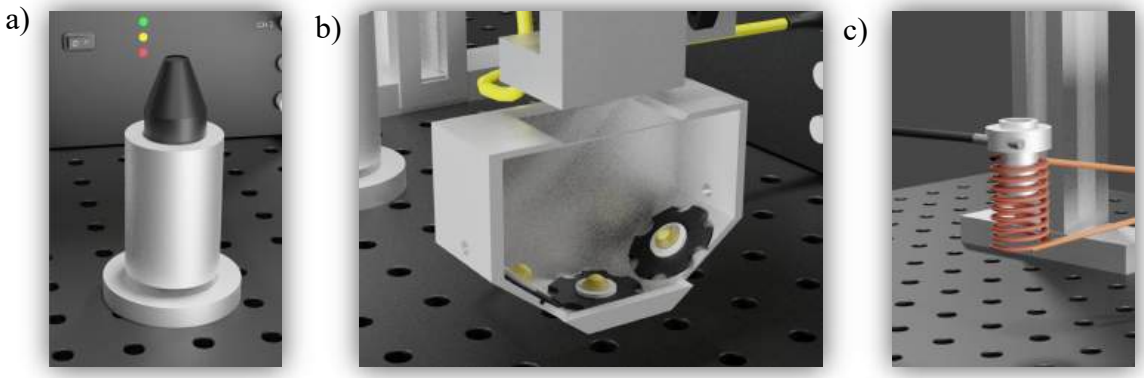

Figure 46. a) Polymer deposit stage, b) UV curing stage, c) temperature curing stage.

The outer diameter of the ferrule connector tip is 2mm; we designed the PLA container with the same top diameter to facilitate the polymer transfer. It is mandatory to accurately place the connector tip in front of the polymer container. Since we used a driver that splits 16 times the steps of the motors, we achieved a displacement resolution of 11 μm per step for each motor. With this configuration, we were allowed to apply microsteps and obtain smooth and precise motion. The polymer transfer process is shown in Fig. 47.

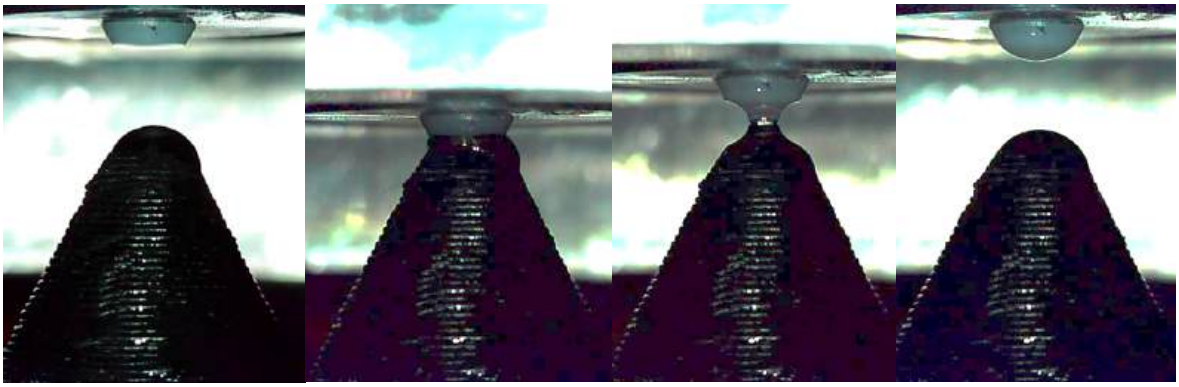

Figure 47. Polymer transfer process on the tip of the connector ferrule.

The entire process of fabricating a tip with NOA81 polymer is shown in Fig. 48. First, the mechanism sets both motors to their origin (Fig. 48(a)), which is an important step. It is difficult to save the position at any point of the fabrication every time the mechanism restarts. Setting the motors to their origin allowed us to place the connector tip in whatever position we wanted by a system of coordinates. Using this system, we can position the connector in the same place we want it to be, no matter how many times the process repeats. Once we knew where the connector was placed, we programmed the path to the PLA container to transfer the polymer (Fig. 48(b)). After that, we placed the connector, now with polymer on the tip, in front of the digital microscope to picture the shape of the polymer tip. The last step was to locate the connector inside the UV curing container for 10 minutes at maximum irradiance to finalize the curing process (Fig. 48(c)).

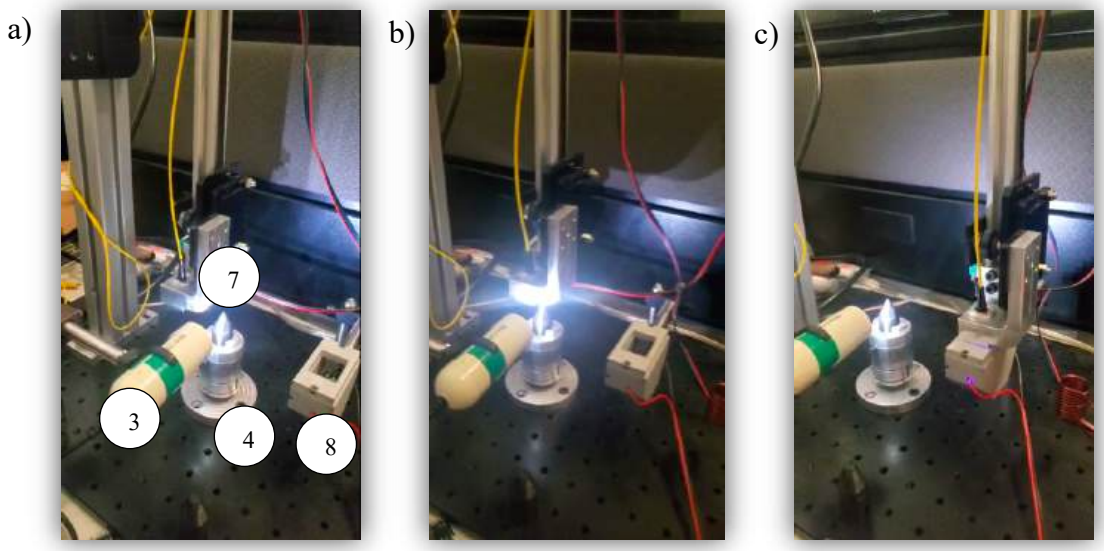

Figure 48. Tip fabrication process using the UV curing stage: a) Setting both motors to the origin, b) polymer transfer process, c) curing process.

The temperature curing process is very similar; every step is shown in Fig. 49. The first and second steps are the origin position of the motors and the polymer transfer, respectively (Figs. 49(a) and 49(b)). The polymer-capped tip must be inside a metal cavity to induct the heating process by the coil. The next step is to screw in an aluminum nozzle that will be at the heating

stage; Fig. 49(c) shows the insertion of the nozzle, and Fig. 49(d) shows an image of the nozzle already placed. The final step is putting the polymer-capped tip with the nozzle inside the coil to start heating (Fig. 49(e)). A thermocouple is attached to the nozzle to measure the increasing temperature; this value is displayed in the LCD, as shown in Fig. 49(f). The curing process lasts up to 1 hour; that is when it reaches 60^{o}C.

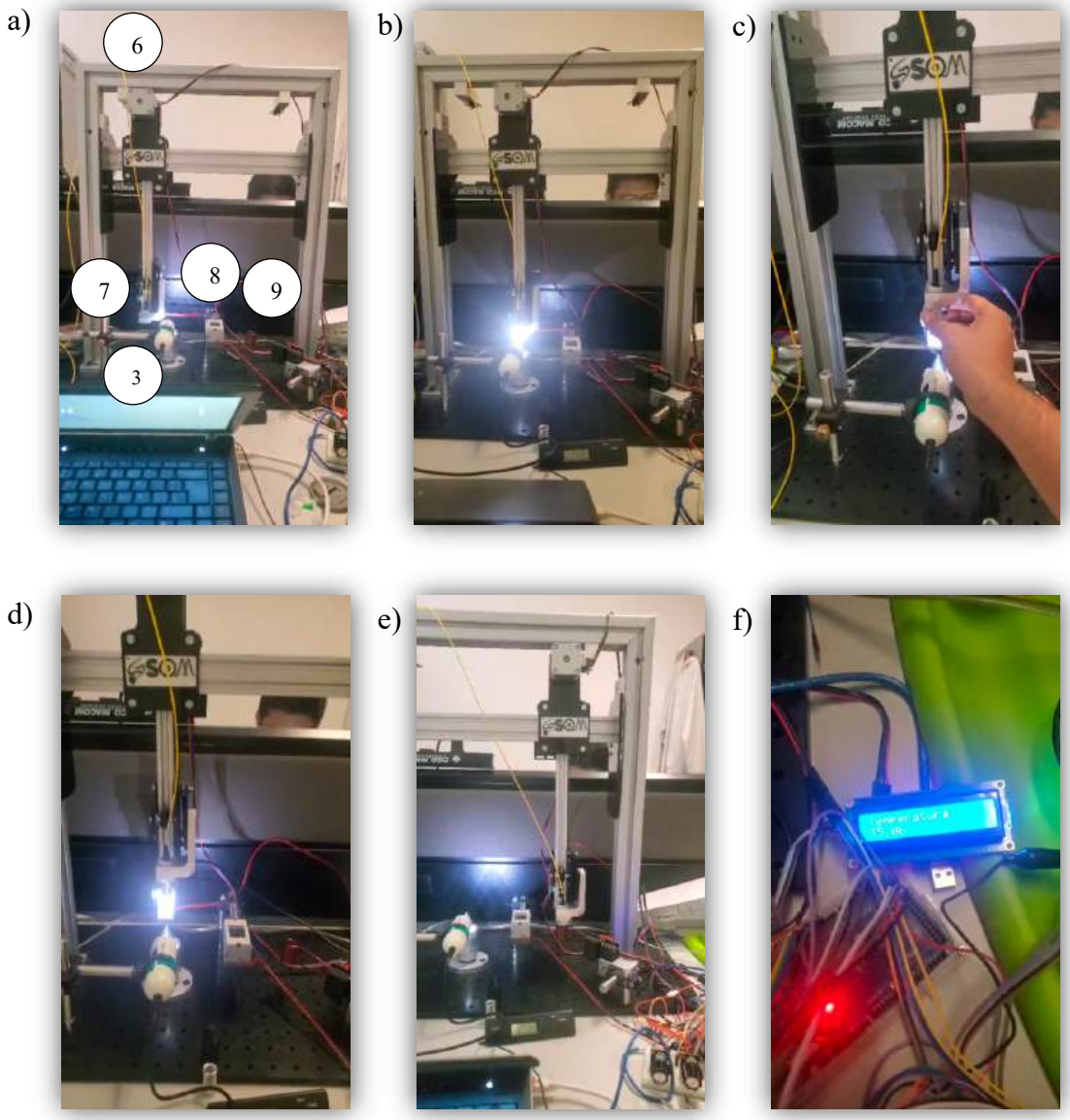

Figure 49. Tip fabrication process using the temperature curing stage: a) Setting both motors to the origin, b) polymer transfer process, c) nozzle insertion, d) nozzle already inserted, e) curing process, f) measured temperature value in the menu display.

Operating any machine needs an interface for the operator. We designed a menu control to order the platform to perform one of the described processes. Fig. 50 shows the flowchart according to the selection between the UV curing process (NOA) and the temperature process (PDMS). We used a rotary encoder to select every option by rotating and pushing it. On the

other hand, the platform can also be operated manually with two more rotary encoders, one for each motor motion; the motor runs a step for each rotation, and the sense of the rotation of the encoder also defines the sense of the step.

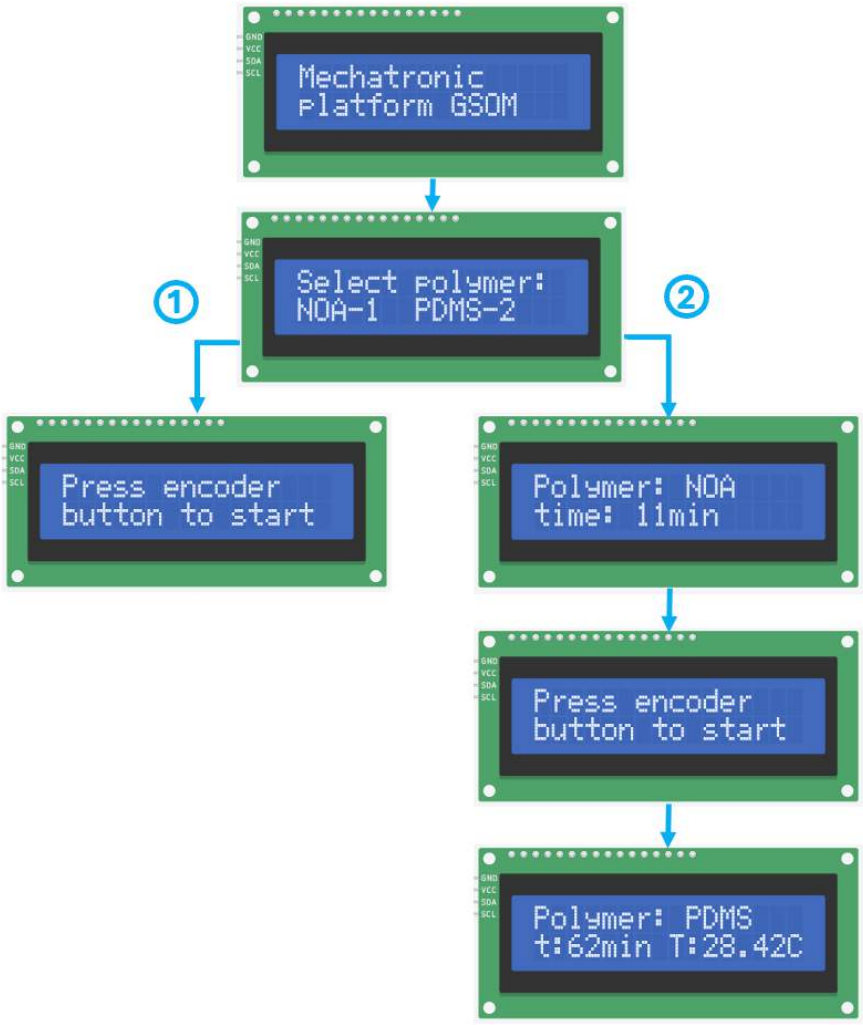

Figure 50. Menu display flowchart with every message displayed depending on the selection made.

We fabricated five tips for each polymer to prove the reproducibility of our machine. First, we present the optical and Fourier spectra for NOA81 in Figs. 51(a) and 51(b), respectively. We obtained five similar spectra with slight differences in the amplitude of their peaks in the Fourier domain. The range of the OPL of the five tips is between 0.4909 mm and 0.5935 mm; having a difference of 0.1026 mm between the shortest and the largest tip. Then, the corresponding optical and Fourier spectra for PDMS are shown in Figs. 52(a) and 52(b). The range of the OPL of the five tips is between 0.3261 mm and 0.4689 mm. This range presents a difference of 0.1428 mm, wider than the NOA81 tips range. In both cases, we achieve a good correlation for every fabricated tip, i.e. a reproducible fabrication method. The next step

for this platform is to implement a method to control the cavity tips dimensions, just as we presented in Chapter 3, but now in an automated way.

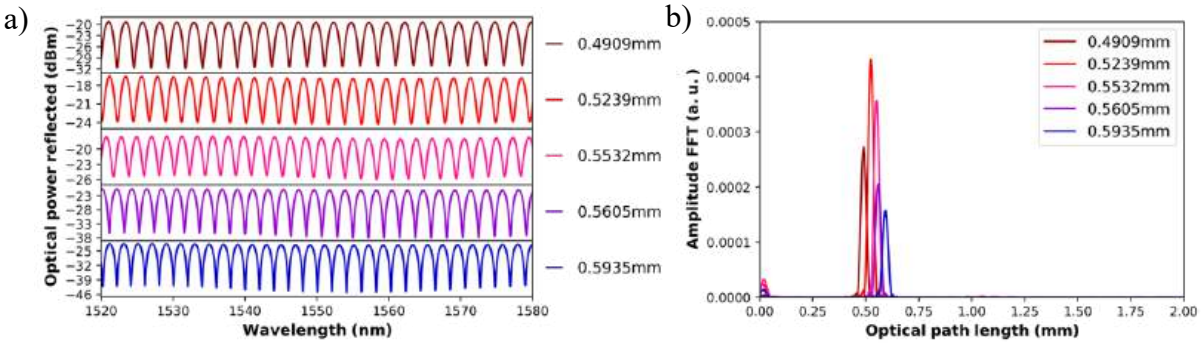

Figure 51. (a) Optical and (b) Fourier spectra of the NOA81 fabricated tips using the mechatronic platform.

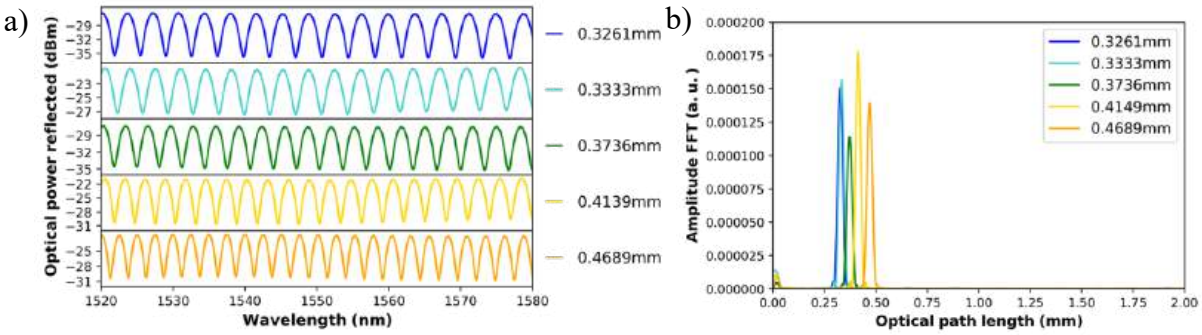

Figure 52. (a) Optical and (b) Fourier spectra of the PDMS fabricated tips using the mechatronic platform.

CHAPTER 7:
CONCLUSIONS

All the research, experimental, and technological development presented in this work was limited by the time. I decided to change my thesis project and advisor halfway through the doctorate, with only 2 years and 2 months left. For this reason, there are many aspects to improve about the mechatronic platform and future research lines to follow to continue from this work.

I designed, developed, and implemented a displacement and temperature sensor using a modified extrinsic Fabry Pérot interferometer with a polymer-capped SMF FC/PC. The displacement sensor is simple to fabricate, exhibits a dynamic range 9 times more extensive than a conventional EFPI, and can detect nanometer displacements using the optical Vernier effect. The temperature sensor increased to 69 times the temperature sensitivity of a traditional EFPI with a polymer cap. I proved the improvement of the dynamic range, sensitivity, and resolution of the reported schemes for measuring distance and temperature by a robust, simple, and easy-to-fabricate alternative FFPI sensor configuration. These results were published in two prestigious scientific journals with a high impact factor.

An automated prototype requires adjustments before, during, and after the manufacturing process and the testing stage. We set up the platform operation according to the three general desired tasks: polymer transfer, UV curing, and temperature curing, all using SMF FC/PC connectors. The future adjustment will be to do the same process but now using bare SMF. Since a stripped fiber has a diameter of 125 μm, we need a different holding piece for the fiber and to program the correct coordinates to place the fiber tip correctly in front of the polymer container and at each stage. The main advantage of creating a specific machine from the beginning is that you can modify its configuration according to the requirements.

The platform reaches a maximum temperature of $60^{o}C$ in one hour. The current of the power source limits this aspect. By changing the power source, we can increase the maximum temperature value. On the other hand, if we want to improve the UV curing stage, we must add more UV LEDs to the container.

Before the implementation of our machine, we used four principal instruments to fabricate the polymer-capped tips; we present them with their corresponding cost at the time they were acquired:

- Digital dry bath myBlock: $12,558 USD
- Norland Opticure LED 200 Light Gun: $37,915 USD
- Motorized Linear Translation Stage: $51,250 USD
- Two-Channel Benchtop Stepper Motor Controller: $50,820 USD

One objective of the fabrication of our platform was to implement these four instruments in a single machine. Considering every acquired component to fabricate this platform, the estimated general cost is $4500 MXN or $220 USD. We can conclude that this is a low-cost prototype with displacements in two ways with a resolution of 11 μm, with a UV irradiator and a heater nozzle, both in a controlled way.

I have a second version of the cavity for the temperature sensor where the PCFPI is inside. The cavity screw has a bipolar motor coupled, which allows us to have a more accurate longitudinal displacement of the mirror instead of doing it manually. This prototype is in the testing stage.

Scientific production is becoming increasingly important in Mexico, but the situation is different concerning technological contributions from the scientific community. Postgraduate students in science, as future researchers, are in the position to change this situation gradually. As with this work, implementing technology in scientific applications is fundamental to my academic training. In this way, scientific research of current interest and high impact in optics that I can generate takes on greater weight using technology developed by my authorship. In this way, the incursion into the development of prototypes for automation applications in the multiple experimental processes developed in optics laboratories represents a line of research that I wish to continue, leading me to the construction of the prototype presented in this work.

REFERENCES

[1] J. Fraden, “Handbook of modern sensors: Physics, designs, and applications,” *Handbook of Modern Sensors: Physics, Designs, and Applications*, pp. 1–758, Jan. 2016, doi: 10.1007/978-3-319-19303-8/COVER.

[2] B. L. B. Hunt, “The Early History of the Thermocouple,” *Platin Met Rev*, vol. 8, no. 1, pp. 23–28, Jan. 1964, doi: 10.1595/003214064X812328.

[3] P. A. BÉLANGER, D. L. HUTT, and K. J. SNELL, “Alexander Graham Bell’s PHOTOPHONE,” *Optics and Photonics News, Vol. 4, Issue 6, pp. 20-25*, vol. 4, no. 6, pp. 20–25, Jun. 1993, doi: 10.1364/OPN.4.6.000020.

[4] J. Hecht, “A short history of laser development,” *Appl Opt*, vol. 49, no. 25, 2010, doi: 10.1364/AO.49.000F99.

[5] G. Cattani, “Technological pre-adaptation, speciation, and emergence of new technologies: how Corning invented and developed fiber optics,” *Industrial and Corporate Change*, vol. 15, no. 2, pp. 285–318, Apr. 2006, doi: 10.1093/ICC/DTJ016.

[6] D. A. Krohn, T. W. MacDougall, and A. Mendez, “Fiber Optic Sensors: Fundamentals and Applications,” *Fiber Optic Sensors: Fundamentals and Applications*, 2014, doi: 10.1117/3.1002910.

[7] M. F. S. Ferreira *et al.*, “Roadmap on optical sensors,” *Journal of Optics*, vol. 26, no. 1, p. 013001, Dec. 2023, doi: 10.1088/2040-8986/AD0E85.

[8] M. A. Putman, J. S. Sirkis, E. J. Friebele, A. D. Kersey, D. D. Brennan, and T. A. Berkoff, “In-line fiber étalon for strain measurement,” *Optics Letters, Vol. 18, Issue 22, pp. 1973-1975*, vol. 18, no. 22, pp. 1973–1975, Nov. 1993, doi: 10.1364/OL.18.001973.

[9] F. Farahi, T. P. Newson, J. D. C. Jones, and D. A. Jackson, “Coherence multiplexing of remote fibre optic fabry-perot sensing system,” *Opt Commun*, vol. 65, no. 5, pp. 319–321, Mar. 1988, doi: 10.1016/0030-4018(88)90094-6.

[10] C. Fabry and A. Pérot, “Sur les franges des lames minces argentées et leur application à la mesure de petites épaisseurs d’air.,” *Ann. Chim. Phys.*, vol. 12, pp. 459–501, 1897.

[11] J. Luo *et al.*, “Fiber optic hydrogen sensor based on a Fabry–Perot interferometer with a fiber Bragg grating and a nanofilm,” *Lab Chip*, vol. 21, no. 9, pp. 1752–1758, May 2021, doi: 10.1039/D1LC00012H.

[12] M. Ding, “Hollow core fibre based Fabry-Perot interferometers with high finesse,” 2022.

[13] Y. M. Sabry, D. Khalil, B. Saadany, and T. Bourouina, “In-plane external fiber Fabry–Perot cavity comprising silicon micromachined concave mirror,” *https://doi.org/10.1117/1.JMM.13.1.011110*, vol. 13, no. 1, p. 011110, Dec. 2013, doi: 10.1117/1.JMM.13.1.011110.

[14] M. A. Ramirez-Hernandez, M. Alonso-Murias, and D. Monzon-Hernandez, “Polymer-Capped Fiber Fabry-Perot Interferometer for Large Range Displacement Sensing,” *Journal of Lightwave Technology*, vol. 42, no. 9, pp. 3430–3437, May 2024, doi: 10.1109/JLT.2024.3357624.

[15] P. C. Beard and T. N. Mills, “Extrinsic optical-fiber ultrasound sensor using a thin polymer film as a low-finesse Fabry–Perot interferometer,” *Applied Optics, Vol. 35, Issue 4, pp. 663-675*, vol. 35, no. 4, pp. 663–675, Feb. 1996, doi: 10.1364/AO.35.000663.
[16] P. F. Goldsmith and IEEE Microwave Theory and Techniques Society., “Quasioptical systems : Gaussian beam quasioptical propagation and applications,” p. 412, 1998.
[17] H. Kogelnik, “On the Propagation of Gaussian Beams of Light Through Lenslike Media Including those with a Loss or Gain Variation,” *Applied Optics, Vol. 4, Issue 12, pp. 1562-1569*, vol. 4, no. 12, pp. 1562–1569, Dec. 1965, doi: 10.1364/AO.4.001562.
[18] Y. M. Sabry, D. Khalil, B. Saadany, and T. Bourouina, “In-plane external fiber Fabry–Perot cavity comprising silicon micromachined concave mirror,” *Journal of Micro/Nanolithography, MEMS, and MOEMS*, vol. 13, no. 1, p. 011110, Dec. 2013, doi: 10.1117/1.JMM.13.1.011110.
[19] Eric. Udd and W. B. . Spillman, “Fiber optic sensors : an introduction for engineers and scientists,” p. 597, 2024.
[20] J. A. Flores-Bravo, M. A. Illarramendi, J. Zubia, and J. Villatoro, “Optical fiber interferometer for temperature-independent refractive index measuring over a broad range,” *Opt Laser Technol*, vol. 139, p. 106977, Jul. 2021, doi: 10.1016/J.OPTLASTEC.2021.106977.
[21] K. N. Amouzou *et al.*, “Development of High Refractive Index Polydimethylsiloxane Waveguides Doped with Benzophenone via Solvent-Free Fabrication for Biomedical Pressure Sensing,” *Photonics 2022, Vol. 9, Page 557*, vol. 9, no. 8, p. 557, Aug. 2022, doi: 10.3390/PHOTONICS9080557.
[22] J. S. Velazquez-Gonzalez, D. Monzon-Hernandez, F. Martinez-Pinon, D. A. May-Arrioja, and I. Hernandez-Romano, “Surface Plasmon Resonance-Based Optical Fiber Embedded in PDMS for Temperature Sensing,” *IEEE Journal of Selected Topics in Quantum Electronics*, vol. 23, no. 2, pp. 126–131, Mar. 2017, doi: 10.1109/JSTQE.2016.2628022.
[23] M. V. Salapaka and S. M. Salapaka, “Scanning Probe Microscopy,” *IEEE Control Syst*, vol. 28, no. 2, pp. 65–83, 2008, doi: 10.1109/MCS.2007.914688.
[24] B. P. Abbott *et al.*, “Observation of gravitational waves from a binary black hole merger,” *Phys Rev Lett*, vol. 116, no. 6, p. 061102, Feb. 2016, doi: 10.1103/PHYSREVLETT.116.061102/FIGURES/4/MEDIUM.
[25] M. J. Biercuk, H. Uys, J. W. Britton, A. P. Vandevender, and J. J. Bollinger, “Ultrasensitive detection of force and displacement using trapped ions,” *Nature Nanotechnology 2010 5:9*, vol. 5, no. 9, pp. 646–650, Aug. 2010, doi: 10.1038/nnano.2010.165.
[26] T. Y. Cosgun *et al.*, “Miniaturised gap sensor using fibre optic Fabry-Perot interferometry for structural health monitoring,” *Optics Express, Vol. 30, Issue 24, pp. 42923-42932*, vol. 30, no. 24, pp. 42923–42932, Nov. 2022, doi: 10.1364/OE.462070.
[27] M. Rajibul Islam, M. Mahmood Ali, M. H. Lai, K. S. Lim, and H. Ahmad, “Chronology of Fabry-Perot Interferometer Fiber-Optic Sensors and Their Applications: A Review,” *Sensors 2014, Vol. 14, Pages 7451-7488*, vol. 14, no. 4, pp. 7451–7488, Apr. 2014, doi: 10.3390/S140407451.

[28] K. Thurner, P. F. Braun, and K. Karrai, “Fabry-Pérot interferometry for long range displacement sensing,” *Review of Scientific Instruments*, vol. 84, no. 9, p. 095005, Sep. 2013, doi: 10.1063/1.4821623.
[29] Y. Zhang *et al.*, “Fringe visibility enhanced extrinsic Fabry-Perot interferometer using a graded index fiber collimator,” *IEEE Photonics J*, vol. 2, no. 3, pp. 469–481, 2010, doi: 10.1109/JPHOT.2010.2049833.
[30] M. C. Alonso-Murias *et al.*, “Long-range multicore optical fiber displacement sensor,” *Optics Letters, Vol. 46, Issue 9, pp. 2224-2227*, vol. 46, no. 9, pp. 2224–2227, May 2021, doi: 10.1364/OL.421004.
[31] C. J. Moreno-Hernández, D. Monzón-Hernández, A. Martínez-Ríos, D. Moreno-Hernández, and J. Villatoro, “Long-range interferometric displacement sensing with tapered optical fiber tips,” *IEEE Photonics Technology Letters*, vol. 27, no. 4, pp. 379–382, Feb. 2015, doi: 10.1109/LPT.2014.2375651.
[32] M. Alonso-Murias, D. Monzón-Hernández, E. Antonio-Lopez, A. Schülzgen, R. Amezcua-Correa, and J. Villatoro, “Hybrid optical fiber Fabry-Perot interferometer for nano-displacement sensing,” *Opt Laser Technol*, vol. 155, p. 108426, Nov. 2022, doi: 10.1016/J.OPTLASTEC.2022.108426.
[33] B. Culshaw and A. Kersey, “Fiber-optic sensing: A historical perspective,” *Journal of Lightwave Technology*, vol. 26, no. 9, pp. 1064–1078, May 2008, doi: 10.1109/JLT.0082.921915.
[34] Y. Liu, X. Li, Y. nan Zhang, and Y. Zhao, “Fiber-optic sensors based on Vernier effect,” *Measurement*, vol. 167, p. 108451, Jan. 2021, doi: 10.1016/J.MEASUREMENT.2020.108451.
[35] A. N. Starodumov, L. A. Zenteno, D. Monzon, and E. De La Rosa, “Fiber Sagnac interferometer temperature sensor,” *Appl Phys Lett*, vol. 70, no. 1, pp. 19–21, Jan. 1997, doi: 10.1063/1.119290.
[36] J. S. Velázquez-González, D. Monzón-Hernández, D. Moreno-Hernández, F. Martínez-Piñón, and I. Hernández-Romano, “Simultaneous measurement of refractive index and temperature using a SPR-based fiber optic sensor,” *Sens Actuators B Chem*, vol. 242, pp. 912–920, Apr. 2017, doi: 10.1016/J.SNB.2016.09.164.
[37] Y. Wang *et al.*, “Novel optical fiber SPR temperature sensor based on MMF-PCF-MMF structure and gold-PDMS film,” *Optics Express, Vol. 26, Issue 2, pp. 1910-1917*, vol. 26, no. 2, pp. 1910–1917, Jan. 2018, doi: 10.1364/OE.26.001910.
[38] I. Hernandez-Romano, D. Monzon-Hernandez, C. Moreno-Hernandez, D. Moreno-Hernandez, and J. Villatoro, “Highly Sensitive Temperature Sensor Based on a Polymer-Coated Microfiber Interferometer,” *IEEE Photonics Technology Letters*, vol. 27, no. 24, pp. 2591–2594, Dec. 2015, doi: 10.1109/LPT.2015.2478790.
[39] I. Hernández-Romano *et al.*, “Optical fiber temperature sensor based on a microcavity with polymer overlay,” *Optics Express, Vol. 24, Issue 5, pp. 5654-5661*, vol. 24, no. 5, pp. 5654–5661, Mar. 2016, doi: 10.1364/OE.24.005654.
[40] L. Liu *et al.*, “Dual Self-Growing Polymer Microtips on a Multicore Fiber for Humidity and Temperature Discriminative Sensing,” *Journal of Lightwave Technology, Vol. 41, Issue 13, pp. 4322-4330*, vol. 41, no. 13, pp. 4322–4330, Jul. 2023, Accessed: Oct. 15, 2023. [Online]. Available: https://opg.optica.org/abstract.cfm?uri=jlt-41-13-4322

[41] W. Yang *et al.*, “Highly sensitive fiber-optic temperature sensor with compact hybrid interferometers enhanced by the harmonic Vernier effect,” *Optics Express, Vol. 31, Issue 9, pp. 14570-14582*, vol. 31, no. 9, pp. 14570–14582, Apr. 2023, doi: 10.1364/OE.485208.
[42] X. Liu *et al.*, “Ultrasensitive temperature sensor with Vernier-effect improved fiber Michelson interferometer,” *Optics Express, Vol. 29, Issue 2, pp. 1090-1101*, vol. 29, no. 2, pp. 1090–1101, Jan. 2021, doi: 10.1364/OE.415857.
[43] C. Shen, B. Mao, D. N. Wang, C. Zhao, B. Xu, and L. Hou, “Highly sensitive PDMS-filled Fabry–Perot interferometer temperature sensor based on the Vernier effect,” *Applied Optics, Vol. 58, Issue 18, pp. 4858-4865*, vol. 58, no. 18, pp. 4858–4865, Jun. 2019, doi: 10.1364/AO.58.004858.
[44] X. Y. Zhang *et al.*, “Miniature end-capped fiber sensor for refractive index and temperature measurement,” *IEEE Photonics Technology Letters*, vol. 26, no. 1, pp. 7–10, Jan. 2014, doi: 10.1109/LPT.2013.2286260.
[45] B. Sun *et al.*, “Simultaneous measurement of pressure and temperature by employing Fabry-Perot interferometer based on pendant polymer droplet,” *Optics Express, Vol. 23, Issue 3, pp. 1906-1911*, vol. 23, no. 3, pp. 1906–1911, Feb. 2015, doi: 10.1364/OE.23.001906.
[46] O. Arrizabalaga, G. Durana, J. Zubia, and J. Villatoro, “Accurate microthermometer based on off center polymer caps onto optical fiber tips,” *Sens Actuators B Chem*, vol. 272, pp. 612–617, Nov. 2018, doi: 10.1016/J.SNB.2018.05.148.
[47] A. M. Velázquez-Benítez, J. Hernández-Cordero, R. Defas-Brucil, and M. S. Cano-Velázquez, “Microbubble end-capped fiber-optic Fabry–Perot sensors,” *Optics Letters, Vol. 47, Issue 21, pp. 5569-5572*, vol. 47, no. 21, pp. 5569–5572, Nov. 2022, doi: 10.1364/OL.474208.
[48] O. Bang *et al.*, “Thermal Profile Detection Through High-Sensitivity Fiber Optic Chirped Bragg Grating on Microstructured PMMA Fiber,” *Journal of Lightwave Technology, Vol. 36, Issue 20, pp. 4723-4729*, vol. 36, no. 20, pp. 4723–4729, Oct. 2018, Accessed: Nov. 15, 2023. [Online]. Available: https://opg.optica.org/abstract.cfm?uri=jlt-36-20-4723
[49] J. M. López-Higuera, L. R. Cobo, A. Q. Incera, and A. Cobo, “Fiber optic sensors in structural health monitoring,” *Journal of Lightwave Technology*, vol. 29, no. 4, pp. 587–608, 2011, doi: 10.1109/JLT.2011.2106479.
[50] R. Min, Z. Liu, L. Pereira, C. Yang, Q. Sui, and C. Marques, “Optical fiber sensing for marine environment and marine structural health monitoring: A review,” *Opt Laser Technol*, vol. 140, p. 107082, Aug. 2021, doi: 10.1016/J.OPTLASTEC.2021.107082.
[51] J. Zubia, J. Villatoro, and O. Arrizabalaga, “Microrefractometer Based on Off-Center Polymer Caps Bonded Onto Optical Fiber Tips,” *Journal of Lightwave Technology, Vol. 36, Issue 17, pp. 3573-3579*, vol. 36, no. 17, pp. 3573–3579, Sep. 2018, Accessed: Oct. 15, 2023. [Online]. Available: https://opg.optica.org/abstract.cfm?uri=jlt-36-17-3573
[52] H. Gao, H. Hu, Y. Zhao, J. Li, M. Lei, and Y. Zhang, “Highly-sensitive optical fiber temperature sensors based on PDMS/silica hybrid fiber structures,” *Sens Actuators A Phys*, vol. 284, pp. 22–27, Dec. 2018, doi: 10.1016/J.SNA.2018.10.011.
[53] Y. Yang, Y. Wang, Y. Zhao, and J. Jiang, “Ultrasensitive Temperature Sensor Based on Fiber-Optic Fabry–Pérot Interferometer with Vernier Effect,” *Journal of Russian*

Laser Research, vol. 40, no. 3, pp. 243–248, May 2019, doi: 10.1007/S10946-019-09796-2/METRICS.

[54] M. qing Chen, Y. Zhao, F. Xia, Y. Peng, and R. jie Tong, "High sensitivity temperature sensor based on fiber air-microbubble Fabry-Perot interferometer with PDMS-filled hollow-core fiber," *Sens Actuators A Phys*, vol. 275, pp. 60–66, Jun. 2018, doi: 10.1016/J.SNA.2018.03.044.

[55] R. Pan *et al.*, "High-sensitive temperature sensor with parallel PDMS-filled FPIs based on dual Vernier effect," *Opt Commun*, vol. 518, p. 128284, Sep. 2022, doi: 10.1016/J.OPTCOM.2022.128284.

[56] M. Dai *et al.*, "Fiber Optic Temperature Sensor with Online Controllable Sensitivity Based on Vernier Effect," *IEEE Sens J*, vol. 21, no. 19, pp. 21555–21563, Oct. 2021, doi: 10.1109/JSEN.2021.3101572.

[57] J. He *et al.*, "Highly Sensitive Temperature Sensor Based on Cascaded Polymer-Infiltrated Fiber Mach–Zehnder Interferometers Operating near the Dispersion Turning Point," *Polymers 2022, Vol. 14, Page 3617*, vol. 14, no. 17, p. 3617, Sep. 2022, doi: 10.3390/POLYM14173617.

[58] M. Ramírez-Hernández, M. Alonso-Murias, and D. Monzón-Hernández, "Highly Sensitive Temperature Sensor Based on Vernier Effect Using a Sturdy Double-cavity Fiber Fabry-Perot Interferometer," *Polymers 2023, Vol. 15, Page 4567*, vol. 15, no. 23, p. 4567, Nov. 2023, doi: 10.3390/POLYM15234567.